electronics

MDPI

Article

A Novel HOT-STA-SMC Strategy Integrated with MRAS for High-Performance Sensorless PMSM Drives

Djaloul Karboua [1], Said Benkaihoul [2], Abdelkader Azzeddine Bengharbi [3] and Francisco Javier Ruiz-Rodríguez [4,*]

[1] Laboratory of Renewable Energy Systems Applications (LASER), Department of Electrical Engineering, Faculty of Science and Technology, Ziane Achour University, Djelfa 17000, Algeria; djaloul.karboua@univ-djelfa.dz
[2] Laboratory of Applied Automation and Industrial Diagnostics (LAADI), Department of Electrical Engineering, Faculty of Science and Technology, Ziane Achour University, Djelfa 17000, Algeria; saidbenkaihoul@gmail.com
[3] Department of Electrical Engineering, El Oued University, El Oued 39000, Algeria; bengharbi-aek-azz@univ-eloued.dz
[4] Research Center in Technology, Energy and Sustainability (CITES), Department of Electrical and Thermal Engineering, University of Huelva, 21007 Huelva, Spain
* Correspondence: javier.ruiz@die.uhu.es

Abstract

This paper proposes an advanced sensorless control strategy for Permanent Magnet Synchronous Motors (PMSMs) aimed at enhancing dynamic performance, robustness, and reliability while eliminating the need for mechanical sensors. The core contribution lies in a novel hybrid speed regulation framework that combines a terminal sliding mode control scheme with a high-order super-twisting algorithm (HOT-STA-SMC), ensuring finite-time convergence, effective chattering suppression, and strong disturbance rejection under varying operating conditions. For the inner current loop, an Exponential Reaching Law Sliding Mode Controller (ERL-SMC) is implemented to guarantee fast current response and precise current tracking, even in the presence of parameter uncertainties. Furthermore, the conventional Model Reference Adaptive System (MRAS) observer is embedded within the proposed control architecture, resulting in more accurate speed estimation and enhanced stability during load fluctuations. The complete control system is rigorously modeled and tested in MATLAB R2024b/Simulink, capturing the full interaction between machine dynamics, control loops, and observer mechanisms. The simulation results verify that the proposed design achieves superior torque smoothness, minimal current ripples, and fast transient response compared to conventional sensorless methods. By integrating high-order sliding modes with advanced adaptive observation, this work offers a robust and cost-effective solution for high-performance PMSM drives, suitable for demanding applications such as electric vehicles, renewable energy conversion, and industrial motion control.

Keywords: sensorless speed; MRAS; robust control; nonlinear control; STA; TSMC; High Order Sliding Surface; PMSM; ERL

Academic Editor: Fabio Corti

Received: 20 January 2026
Revised: 28 February 2026
Accepted: 2 March 2026
Published: 6 March 2026

1. Introduction

1.1. General Context and Motivation

Permanent Magnet Synchronous Motors (PMSMs) have emerged as a cornerstone technology in modern motion control systems, increasingly powering applications that demand

high efficiency, compact size, and precise performance. From electric vehicles and renewable energy systems to advanced robotics and aerospace technologies, PMSMs are favored for their superior power density, reduced losses, and excellent dynamic characteristics, all of which contribute to improved energy utilization and operational reliability. Unlike traditional induction motors, PMSMs employ rotor-mounted permanent magnets that generate the magnetic field without the need for external excitation, minimizing mechanical wear and lowering maintenance requirements over their operational lifespan [1–4].

1.2. Problem Statement and Boundaries

However, to fully harness these advantages, PMSMs must be controlled or observed with high accuracy and robustness. Their inherent nonlinearity, strong coupling, and multivariable behavior require sophisticated strategies to deliver the precise speed and current responses essential for critical applications such as high-performance drives, industrial automation, and precision robotics. Control or observer configurations have become the dominant approach for managing PMSMs, allowing decoupled control of speed and current components to ensure fast dynamic response and steady-state accuracy [2,4].

Traditionally, these control strategies rely on mechanical sensors to measure rotor speed and position. While effective, such sensors add to system cost and complexity, occupy valuable installation space, and can reduce overall reliability due to potential failures or degradation in harsh environments. To address these challenges, sensorless control techniques have been widely investigated to estimate rotor speed and position from electrical signals, eliminating the need for physical sensors. Despite significant progress, conventional sensorless methods often struggle to maintain high estimation accuracy and disturbance rejection capability, particularly under parameter uncertainties, low-speed operation, or sudden load variations. These limitations underscore the need for advanced sensorless control solutions that can deliver reliable, high-performance operation while minimizing system cost and maintenance demands [5,6].

1.3. Background on Control and Sensorless Speed Configurations

The control configurations developed for PMSMs are generally classified into two principal categories: scalar control and vector control. Scalar control, known for its simplicity and ease of implementation, delivers acceptable steady-state performance but suffers from inherently slow dynamic response, making it less suitable for high-performance applications. To overcome these limitations and achieve precise dynamic and steady-state behavior, modern systems predominantly adopt closed-loop vector control strategies. Vector control forms the backbone of advanced PMSM drives and encompasses both conventional and modern control schemes. The conventional category mainly relies on proportional–integral–derivative (PID) controllers or hysteresis regulators, as typified by widely used methods like Field Oriented Control (FOC) and Direct Torque Control (DTC). In contrast, advanced vector control techniques branch into nonlinear, optimal, adaptive, and artificial intelligent strategies, each distinguished by its control objectives, modeling requirements, and design complexity. Nonlinear methods, such as Sliding Mode Control (SMC), Backstepping Control (BSC), Passivity-Based Control (PBC), and Feedback Linearization Control (FBLC), directly handle the PMSM's inherent nonlinearities without resorting to model simplification. Optimal controllers, including Model Predictive Control (MPC) and Linear Quadratic Regulator (LQR), focus on performance indices to optimize dynamic behavior and energy efficiency. Adaptive control methods, like Model Reference Adaptive Control (MRAC), adapt parameters in real time and can be implemented in direct, indirect, or command-matching forms to cope with system uncertainties. Furthermore, artificial intelligent control approaches such as Fuzzy Logic Control (FLC), Artificial Neural Networks (ANN), and

Genetic Algorithms (GA) and others are increasingly integrated to enhance traditional techniques or to enable data-driven decision-making, providing greater flexibility and robustness in complex operating conditions [2,4,7,8]. A comprehensive overview of these control strategies for PMSM drives is illustrated in Figure 1.

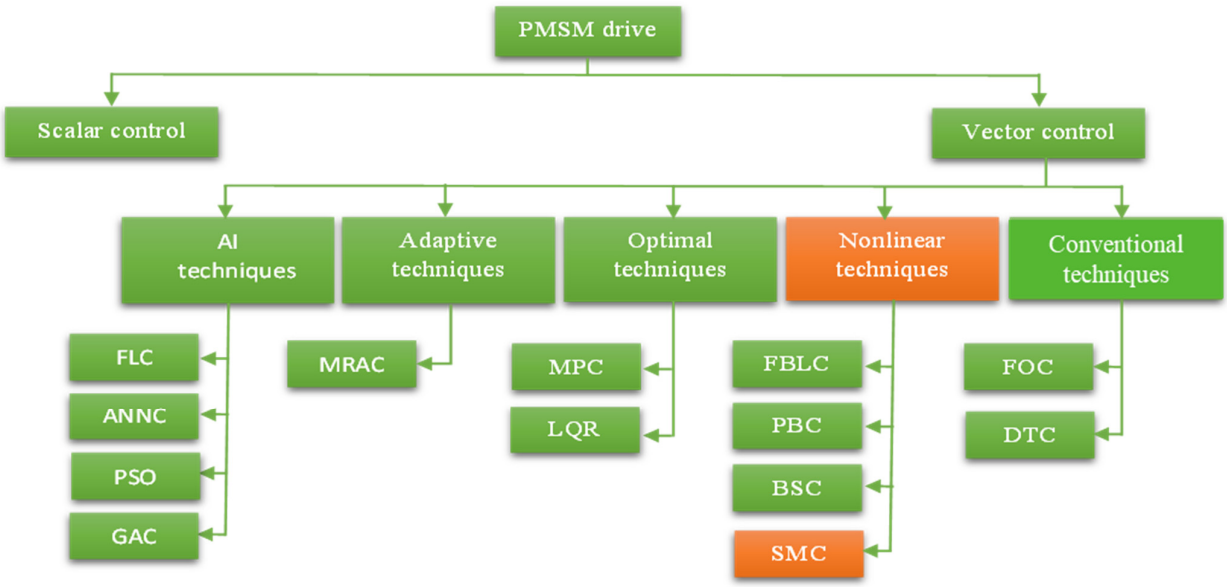

Figure 1. Classification of Control Strategies for PMSM Drives.

Sensorless speed configurations for PMSMs are broadly categorized according to their operational principles and speed range applicability. Fundamentally, these techniques aim to estimate the rotor position and speed using only electrical measurements, thereby eliminating the need for mechanical sensors and improving system cost-effectiveness, reliability, and durability in harsh environments. Sensorless methods can be divided into two main groups: model-based and non-model-based approaches. Model-based methods are predominantly employed in the medium- to high-speed operating ranges and can be further classified into non-adaptive estimators and adaptive observers. Non-adaptive estimators directly infer machine states such as back-EMF or flux without compensating for modeling errors, making them more sensitive to parameter variations. In contrast, adaptive observers introduce correction mechanisms to reconcile discrepancies between measured and predicted quantities, thereby enhancing robustness against parameter uncertainties. Representative examples include the Extended Kalman Filter (EKF), Luenberger Observer (LO), Sliding Mode Observer (SMO), and Model Reference Adaptive System (MRAS). For the challenging zero- to low-speed range, saliency-based methods, also known as High-Frequency Model (HFM) techniques, exploit rotor anisotropy by injecting high-frequency signals to deduce position information, though they can introduce torque ripple. Complementing these physics-based methods, non-model-based techniques leveraging artificial intelligence, such as fuzzy logic, neural networks, and machine learning algorithms, are increasingly applied in medium- and high-speed regimes to enhance estimation accuracy without needing an explicit machine model. Collectively, these configurations aim to balance precision, computational complexity, and implementation practicality, ensuring robust and reliable speed estimation for advanced PMSM drive systems [9–12]. To visually summarize these configurations, Figure 2 presents a comprehensive scheme outlining the classification of sensorless speed for PMSM systems.

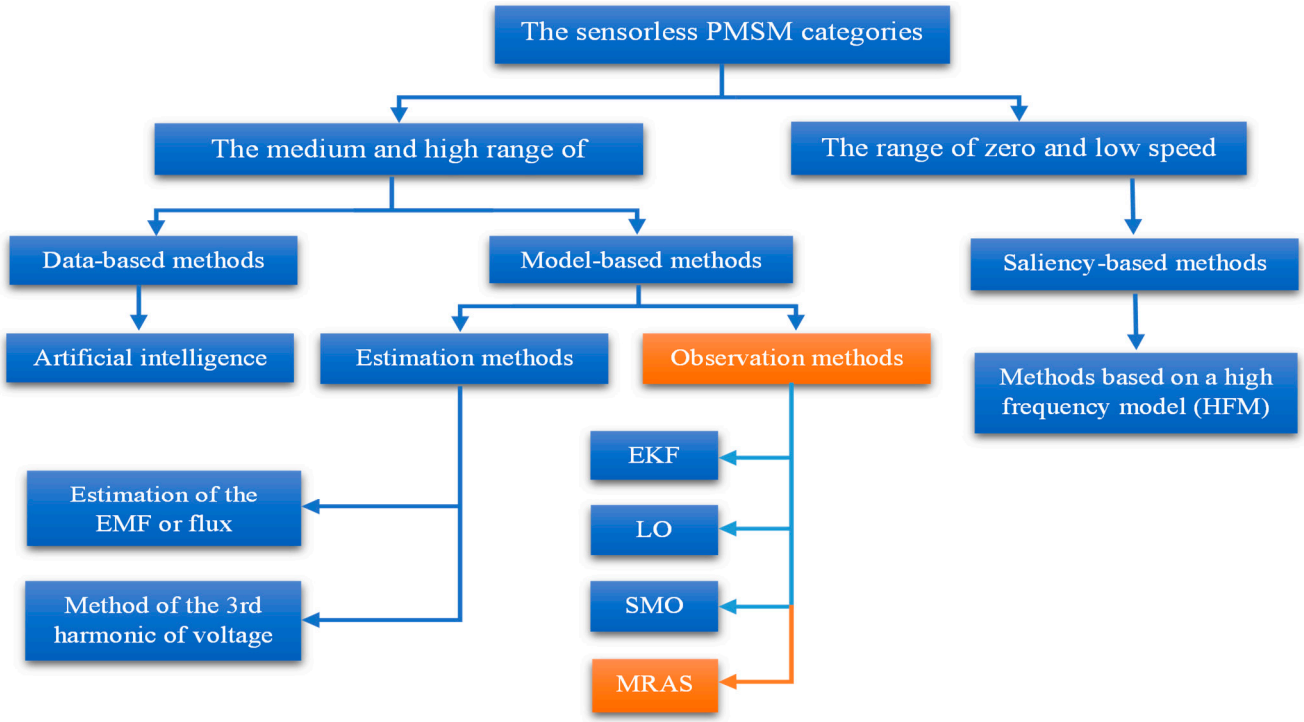

Figure 2. Categorization of Sensorless Speed configuration for PMSMs.

SMC can be broadly classified into four principal categories that address its performance enhancement and practical implementation challenges. The Pseudo-Sliding Mode (PSM) category mainly includes techniques such as the boundary layer approach and the use of approximate functions to smooth control actions and reduce chattering. Similarly, the Approach Reaching Law (ARL) modifies the trajectory by introducing convergence laws such as UAL, PAL, ERL, or sophisticated algorithms like the Twisting Algorithm and Super Twisting Algorithm (STA), all aiming to ensure smoother transitions to the sliding surface and lower oscillations. The High-Order Design category enhances classic SMC by incorporating advanced strategies such as Integral design, Terminal strategy, and Fast-Terminal strategy, which improve convergence speed and robustness. Finally, the Hybridization Method integrates SMC with other control paradigms, combining it with adaptive techniques (estimation), optimal techniques (cost function-based), nonlinear techniques (Lyapunov candidate functions), or intelligent techniques (such as fuzzy logic, neural networks, or particle swarm optimization) [4,13–16]. This classification, summarized in Figure 3, highlights the main development paths for improving SMC performance, mitigating chattering, and expanding its practical applications.

1.4. Literature Review

Achieving high-performance control of PMSMs remains a persistent challenge, particularly with conventional techniques like FOC and DTC, which are often limited by sensitivity to parameter variations and high torque ripple. To overcome these drawbacks and enhance the overall performance of PMSM drives, numerous studies have focused on nonlinear control strategies such as BSC, FBLC, and PBC. These techniques have demonstrated notable robustness under various demanding conditions and have been widely applied to address system nonlinearities and uncertainties. FBLC has frequently been combined with field weakening strategies to extend the speed range, while BSC has been improved through IBSC to reduce steady-state errors and enhance disturbance rejection. PBC, based on energy-shaping principles, has also gained attention for ensuring system stability. Despite their advantages, they still require further development to achieve higher

levels of PMSM performance and ensure complete robustness under the most severe and dynamic operating scenarios [17–20].

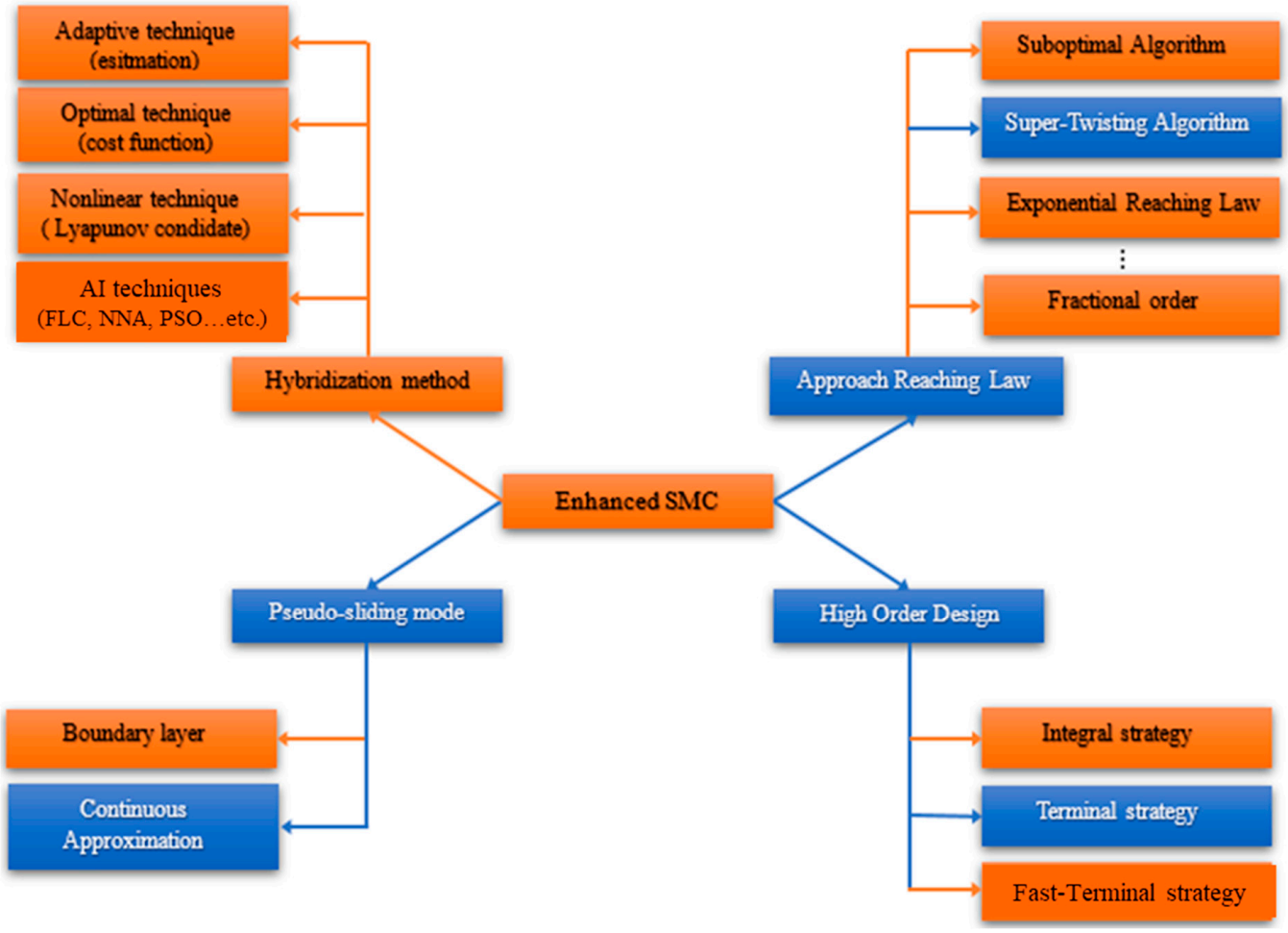

Figure 3. Classification of Enhanced SMC Strategies for PMSM Drives.

Numerous researchers have endeavored to mitigate the persistent issues associated with SMC by introducing various enhancements. For instance, the works presented in [21–24] employed a SMC incorporating an exponential reaching law alongside a sigmoid function. This combination effectively alleviated the chattering phenomenon near the sliding surface, with the exponential law and sigmoid profile contributing to improved switching dynamics and robustness. However, this approach resulted in a partial compromise of the system's convergence stability. Meanwhile, studies in [25,26] aimed to minimize steady-state errors and accelerate the dynamic response of PMSMs by integrating the system's state variables into the sliding surface, thereby forming an integral sliding mode structure. Although this method enhanced robustness against load disturbances, it led to noticeable overshoots due to integral saturation, which undermines controller performance. In a separate line of work, articles [27,28] proposed terminal sliding mode control to achieve rapid and finite-time convergence. Despite its strengths, this method exhibited reduced dynamic performance when the system state was distant from the equilibrium, leading to prolonged convergence. To overcome such shortcomings, other researchers proposed hybrid controllers combining SMC with intelligent, optimal, or adaptive techniques. A notable example is found in [29], which presents a control scheme merging exponential SMC for the speed loop with passivity-based control for the d-q current loop. Although

this hybrid controller demonstrated performance gains over standard SMC, it still suffered from undershoot during disturbances.

Similarly, the design proposed in [30] integrated a non-singular super-twisting algorithm (NSTA) into the speed loop, retaining FOC for the current loop. The inclusion of adaptive and proportional terms addressed limitations of the conventional super-twisting method, such as slow convergence and weak disturbance rejection. Nevertheless, the controller continued to show overshoot and undershoot at high speeds, and the use of FOC exposed the system to parameter sensitivity, notably resistance variations.

Further, the studies [31,32] explored hybrid designs combining SMC with BSC, which provided relatively robust speed regulation under uncertainties. However, this method did not eliminate chattering and showed performance degradation during abrupt speed and torque changes.

Additional contributions include super-twisting SMC integrated with intelligent PI control [33], adaptive algorithms based on super-twisting sliding mode [34], fractional-order SMC approaches, combination of the optimal such as MPC and LQR with SMC, intelligent sliding mode control [35–38]. Collectively, these sustained research efforts demonstrate that SMC remains a cornerstone of robust nonlinear control for PMSM applications. Yet, theorical and practical deployments still face challenges related to residual chattering, overshoot, and sensitivity to parameter drift, especially at high speeds or under varying load conditions. As the literature shows, refining and hybridizing SMC with advanced estimation, learning, and optimization techniques remains vital for realizing next-generation PMSM drives that combine precision, efficiency, and resilience in real-world scenarios.

Within sensorless speed configurations for the PMSM, EKF remains a prevalent observer due to its ability to estimate rotor speed and position from current and voltage signals. However, it is highly sensitive to tuning of noise covariance matrices, affecting estimation accuracy and stability. One study used Recursive Least Squares (RLS) with a forgetting factor and Variable-Scale Chaotic PSO (VCPSO) for identifying noise matrices, showing better speed and accuracy than standard PSO variants [39]. Similarly, Biogeography-Based Optimization (BBO) showed superior convergence and estimation performance over PSO and GA for tuning EKF's Q and R matrices under dynamic loads [40], though both rely on offline metaheuristics, limiting real-time adaptability. To improve EKF in complex scenarios, hybrid methods have been proposed. One combined SMC with Whale Optimization and used EKF enhanced by Gaussian Process Regression (GPR) to tune switching gains and noise covariance via learned models, achieving robust performance under varying load and speed [41], though GPR adds computational cost. Another integrated EKF with immune mechanism-based PSO and improved SMC laws for better robustness and load disturbance rejection [42], but responsiveness can suffer from EKF delay and multi-level control structure. An advanced method combined EKF with MPC, using stator current measurements alone. UKF estimated rotor position, speed, and torque, feeding MPC to control telescope mount systems at low speed [12]. This dual-layered structure performed well in practice but adds algorithmic load, challenging for high-speed industrial uses. Overall, EKF-based methods are evolving, yet face issues like computational burden, delay sensitivity, and limited real-time adaptability.

SMO techniques have gained prominence in PMSM sensorless control due to their robustness against parameter uncertainties and strong disturbance rejection. However, conventional SMOs often suffer from chattering and limited accuracy, particularly at medium to high speeds. To enhance estimation precision and tracking robustness, one study proposed an improved adaptive super-twisting SMO (LSTA-SMO) with a speed-dependent sliding mode coefficient and adaptive back-EMF adjustment. This design incorporated a

third-order Extended State Observer (ESO) to estimate mechanical states more accurately, reducing position and speed errors at high velocity while enhancing anti-interference capacity [43]. Another contribution tackled chattering and phase lag by integrating a continuous control function and an adaptive EMF observer structure, combining SMO with a Phase-Locked Loop (PLL) to stabilize sensorless estimation at high speeds. Simulation and experimental results confirmed improved dynamic response and stability [44]. Despite these improvements, challenges such as back-EMF harmonic interference and PLL synchronization under load variations remain areas for further enhancement. In parallel, adaptive gain and switching law redesign have been explored to mitigate SMO limitations. One approach introduced an adaptive sliding mode observer with a continuous saturation function and an explicit Lyapunov-based stability condition. The observer effectively suppressed chattering due to sliding gain mismatch and expanded the observable speed range. Furthermore, it addressed the position estimation delay issue in SMOs with continuous switching functions by proposing a frequency-domain compensation strategy, which significantly enhanced estimation accuracy and real-time performance [45]. Similarly, another work presented an Adaptive Super-Twisting SMO (AST-SMO) with a fast high-order sliding function and adaptive tracking design [46]. Nonetheless, both methods, while powerful in simulation environments, may encounter challenges related to adaptive gain tuning complexity and implementation overhead in real-time systems. To further address torque ripple and speed fluctuation, a super-twisting SMO was coupled with Iterative Learning Control (ILC) and enhanced using fuzzy neural networks (FNNs) for online adaptation. This hybrid controller enabled precise online compensation of q-axis current and achieved superior speed tracking, with effective suppression of periodic oscillations and torque vibration [47]. In another related contribution, the sliding mode reaching law was optimized and applied to both observer and speed controller design, reducing chattering range and demonstrating a smooth dynamic performance improvement over traditional SMO approaches [48]. These strategies underscore the growing trend of integrating machine learning, adaptive laws, and intelligent control with SMO structures. However, the added algorithmic complexity and training dependency may limit real-time applicability or scalability in cost-sensitive industrial environments.

LO-based sensorless control has recently improved PMSM drive performance. One method used second-order Active Disturbance Rejection Control (ADRC) with LO and PLL to enhance disturbance rejection and reduce steady-state errors compared to PI control [49]. Another compared a Luenberger back-EMF observer in FOC to a V/f loop; while the latter is parameter-independent and simpler, LO-FOC offered better precision but required high-performance hardware due to complexity [50]. These show LO's effectiveness but also its parameter sensitivity and low-speed performance limits without advanced signal processing. HFI-based sensorless PMSM control has progressed, especially in AMB systems where physical sensors risk rotor damage. One method used high-frequency square-wave injection (HFSWSII) and pulse-array current injection to avoid filtering delays and improve speed estimation [51]. Another addressed harmonic and gain errors in HFI-based drives via a rotor observer extracting negative high-frequency components, improving low-speed position tracking [52]. To reduce acoustic noise and vibration from harmonics, a novel synchronized modulation method aligned SVPWM and injected signal frequencies, dispersing harmonics and enhancing estimation accuracy with PLL [53]. HFI excels at low speed but faces signal distortion, harmonic sensitivity, and complex tuning in practice.

ESO-based observers enhance PMSM robustness to uncertainties and disturbances. One study proposed a parameter-tuning-free two-step mechanical parameter identification approach based on signal injection and algebraic estimation, enabling accurate identification of nonlinear friction, inertia, and time-varying load torque without observer gain design

or pole placement [54]. Another designed a differentiated ESO with quadrature PLL and adaptive RLS, compensating DC offsets and improving robustness [55]. A third used linear ESO (ELESO) with integral backstepping and dual observers to mitigate flux harmonics and inverter nonlinearity [56]. Yet, ESO methods can amplify noise in differentiation and demand careful gain tuning for stable real-time use.

Recent advancements in sensorless control of PMSMs have introduced various MRAS-based techniques to improve robustness against parameter uncertainties and environmental variations. One innovative approach incorporates fractional-order control into MRAS design, enhancing the estimation of rotor speed and position by adapting to parameter fluctuations and load disturbances across a wide speed range. The design includes a fractional-order model reference adaptive controller (FOMRAC) and an improved observer to suppress chattering and compensate for rotor position errors, thereby improving stability. Simulation results confirm the effectiveness of this fractional-order MRAS in delivering high-precision estimates, especially under variable-speed and variable-load conditions [57]. Another promising direction integrates moving horizon estimation (MHE) with MRAS to form a hybrid observer structure. The MRAS is used for online identification of PMSM parameters such as resistance and inductance, while MHE handles the nonlinear system modeling and robust estimation of rotor position and speed. To address the traditionally high computational burden of MHE, the method is optimized using a Hessian matrix and gradient vector for efficient single-step iterations. The resulting hybrid observer achieves significantly reduced estimation errors compared to classical methods, offering superior adaptability and noise resilience in real-time sensorless control applications [58]. Additionally, researchers have proposed neural network-assisted MRAS observers to tackle the challenges posed by parameter dependency in conventional MRAS techniques. Using an Adaline neural network for online parameter identification and compensation, this scheme significantly improves the accuracy of rotor speed and position estimation, achieving up to 96% error reduction in rotor angle estimation compared to traditional methods [59]. Complementarily, a hybrid scheme that combines MRAS with pseudo-sliding mode control based on the ERL has been developed to address chattering and ensure fast convergence. This fusion of adaptive and nonlinear control provides smoother signals and robust tracking performance under various disturbances, demonstrating excellent dynamic response and resilience in PMSM systems [60]. Despite these notable enhancements, MRAS techniques still suffer from noticeable ripple in electromagnetic torque and stator currents, which can degrade control smoothness and overall system efficiency in high-performance applications.

1.5. Limitations in the Literature

Although extensive research has significantly advanced the control and observation of PMSM drive systems, existing strategies continue to exhibit key technical limitations when it comes to achieving simultaneously optimal, robust, and cost-effective performance. While many studies have successfully developed robust controllers or sensorless estimation techniques individually, few have achieved a fully integrated framework that combines both in a synergistic manner. Most control configurations aim to enhance dynamic behavior and disturbance rejection, yet they often assume the availability of accurate speed and position measurements or rely on mechanical sensors, which increase system cost and reduce reliability. Conversely, sensorless techniques seek to eliminate these sensors, but are commonly validated in isolation often retaining conventional control loops for speed and current regulation, which limits the overall system performance. This separation between control design and sensorless observation undermines the full potential of PMSMs, particularly in demanding environments requiring fast response, high efficiency, and broad

operational range. Therefore, there is a pressing need for unified configurations that not only remove dependency on physical sensors but also ensure optimal electromagnetic and dynamic characteristics through advanced, sensorless, and robust control architectures.

1.6. Contribution of This Work

To address the identified gaps and overcome the fragmented nature of existing PMSM research, this work introduces a unified sensorless control architecture that simultaneously enhances robustness, optimizes dynamic behavior, and eliminates reliance on mechanical sensors. The proposed approach integrates a novel hybrid speed regulation scheme based on Terminal Sliding Mode Control merged with a High-Order Super-Twisting Algorithm (HOT-STA-SMC), offering finite-time convergence, strong disturbance rejection, and effective mitigation of chattering issues that have traditionally limited the practicality of high-performance nonlinear control strategies. In parallel, the inner current regulation loop is governed by an Exponential Reaching Law Sliding Mode Controller (ERL-SMC), which ensures rapid and stable current tracking even under model uncertainties and external perturbations.

Crucially, to achieve sensorless operation without compromising estimation accuracy, a refined MRAS observer is embedded within the control loop. This fusion of adaptive observation and high-order nonlinear control enables more precise rotor-speed estimation, enabling the system to operate reliably across a wide range of speeds and load conditions, while significantly reducing implementation cost and complexity by eliminating physical speed sensors. The complete control-observer framework is comprehensively modeled and validated through MATLAB/Simulink simulations, capturing the intricate coupling between PMSM dynamics, control actions, and observation processes.

By achieving both optimal control characteristics and reliable sensorless estimation in a unified framework, this work advances the state of the art in PMSM drive systems, offering a robust, efficient, and scalable solution applicable to electric vehicles, renewable energy systems, and high-precision industrial drives.

1.7. Work Plane

The structure of this paper is shown in Figure 4. Section 1 introduces the research, covering: (a) General Context and Motivation, (b) Problem Statement and Boundaries, (c) Background on Control and Sensorless Speed Configurations, including classifications of control strategies, sensorless speed configurations, and classification of enhanced SMC strategies, (d) Literature Review on control and sensorless approaches for PMSMs, (e) Identified Limitations in Existing Works, and (f) Contribution of This Work. Section 2 presents the Dynamic Modeling and State-Space Representation of the PMSM Drive. Section 3 describes the Conceptual Design of the Proposed Sensorless Control System, including the HOT-STA-SMC strategy, the MRAS-based speed observer, and a stability analysis of the overall scheme. Section 4 provides the Simulation Results and Discussion. Finally, Section 5 concludes the study and outlines future research directions for experimental validation and real-world implementation.

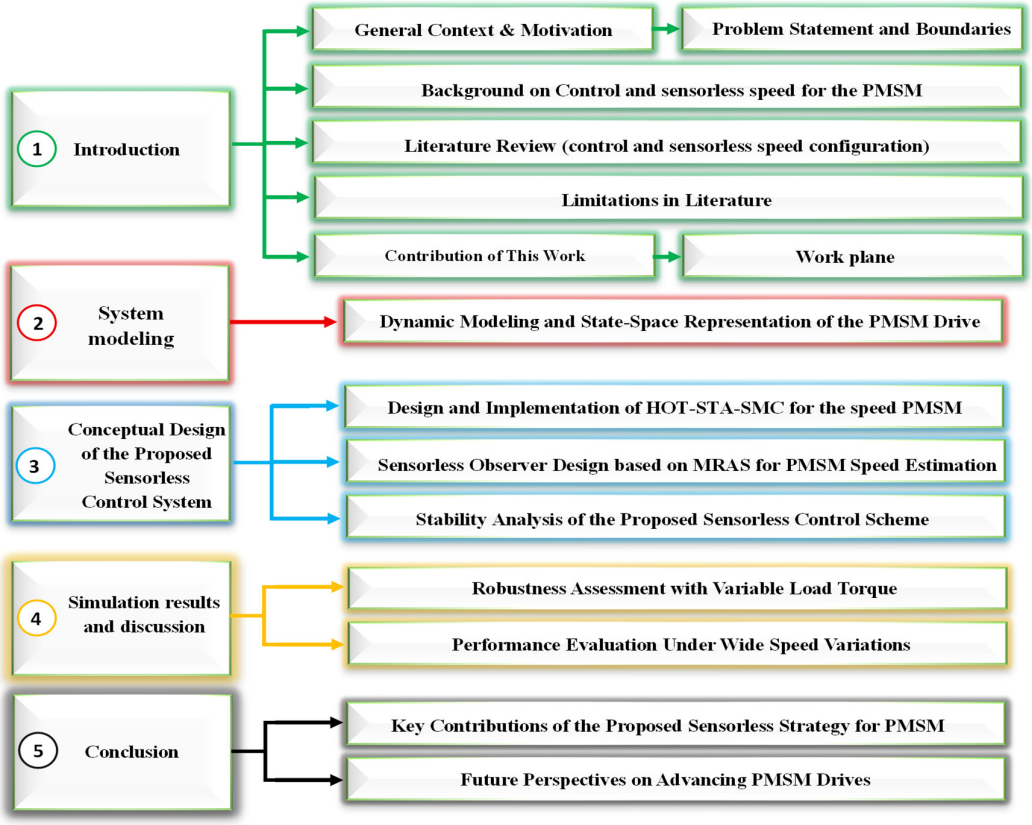

Figure 4. Overview of the Research Structure.

2. Dynamic Modeling and State-Space Representation of the PMSM Drive

PMSMs utilize permanent magnets embedded in the rotor to produce a constant magnetic flux, thereby removing the necessity for an external excitation source. Because of the intrinsic characteristics of the permanent magnet materials, the influence of magnetic saturation is generally ignored in the modeling process. The PMSM exhibits nonlinear dynamics and is subject to various interdependent variables and external disturbances, particularly when analyzed in the rotating d–q coordinate system. Additionally, when equations are transformed into the stationary a–b reference frame, effects like the EMF must be accounted for. Furthermore, losses due to eddy currents and hysteresis are incorporated in the analysis, while the magnetic circuit saturation is omitted for simplification. Considering these factors, the PMSM's dynamic equations can be formulated in the d–q frame, as detailed in [2,4]:

$$\begin{cases} \frac{di_d}{dt} = \frac{1}{L_d}\left(-R_s \cdot i_d - p \cdot L_q \cdot \Omega \cdot i_q + u_d\right) \\ \frac{di_q}{dt} = \frac{1}{L_q}\left(-R_s \cdot i_q - p \cdot L_d \cdot \Omega \cdot i_d - p \cdot \psi_f \cdot \Omega + u_q\right) \\ \frac{d\Omega}{dt} = \frac{1}{j}(T_e - T_l - F \cdot \Omega) \\ \frac{d\theta_r}{dt} = \Omega \end{cases} \quad (1)$$

where $\omega_s = p \cdot \Omega$, and electromagnetic torque is represented by:

$$T_e = \left(3 \cdot \frac{p}{2}\right)\left((L_d - L_q) i_d \cdot i_q + \psi_f \cdot i_q\right) \quad (2)$$

where i_d, i_q are d-q axis equivalent stator currents; u_d, u_q are d-q axis equivalent stator voltages; R_s is per phase stator resistance; L_d, L_q are d-q axis equivalent stator, ω_s and Ω are an electrical (stator) and a mechanical speed; ψ_f is rotor magnetic flux linking the stator,

p is the number of pole pairs; T_e, T_l are electromagnetic and load torques, respectively; j is the moment of inertia of the rotor; F is the friction constant of the rotor and θ_r is the angular speed (electrical position) of the rotor.

3. Conceptual Design of the Proposed Sensorless Control System

This section presents the overall concept of the newly proposed sensorless control design developed for the PMSM drive, which innovatively combines a robust control strategy with an efficient observer scheme. The control configuration employs a HOT-STA-SMC to regulate the speed loop, while the enhanced ERL-SMC ensures precise tracking in the current loop. Complementing this, the observer configuration implements a MRAS for sensorless speed estimation. This MRAS scheme uses the actual speed, current, and voltage signals already shaped by the HOT-STA-SMC and ERL-SMC to generate an accurate speed estimate, which in turn feeds back to the control loops and Park transformation. By closing this mutual loop between the control and observer blocks, the system achieves high-performance speed and current regulation without the need for a physical speed sensor, ensuring both cost-effectiveness and reliable dynamic response. The following subsections detail each configuration and their integrated operation in the proposed sensorless drive system.

3.1. Design and Implementation of HOT-STA-SMC for the Speed PMSM

SMC has established itself as an effective method for controlling PMSMs, mainly due to its notable resilience to parameter deviations and external perturbations, combined with straightforward implementation and rapid response behavior. Nonetheless, the conventional version suffers from the persistent drawback of chattering, which originates from practical issues like detection inaccuracies, switching lags, and system time delays. These limitations can noticeably impair system stability and degrade control precision. Furthermore, the classic SMC design employs a basic linear sliding manifold that can only secure asymptotic convergence, falling short of guaranteeing finite-time state convergence, which is essential for high-performance applications. To overcome these shortcomings, this work presents an enhanced scheme that merges a terminal sliding mode controller with a high-order super-twisting approach (HOT-STA-SMC), exploiting both rapid finite-time tracking and minimized chattering effects. The fundamental idea begins with the definition of a sliding surface [2,7,13–16]:

$$\mathcal{S}(x,t) = \left(\frac{d}{dt} + \lambda\right)^{n-1} e(t) \tag{3}$$

with

$$\frac{1}{2}\cdot\frac{d}{dt}\cdot\mathcal{S}^2 \leq -\eta|\mathcal{S}| \tag{4}$$

where η and λ are strictly positive coefficients, n indicates the system's relative order, and $e(t)$ denotes the speed tracking deviation. For the PMSM, the relevant states are defined by the rotor angle, angular velocity, and its derivative, described by:

$$\begin{cases} x_1 = \theta_r \\ x_2 = \dot{\theta}_r = \Omega \\ x_3 = \ddot{\theta}_r = \dot{\Omega} \end{cases} \tag{5}$$

With the associated error variables formulated as

$$\begin{cases} \mathcal{S}_1 = e_\theta = {\theta_r}^* - \theta_r \\ \mathcal{S}_2 = \dot{e}_\theta = e_\Omega = \Omega^* - \Omega \\ \mathcal{S}_3 = \ddot{e}_\theta = \dot{e}_\Omega \end{cases} \tag{6}$$

where ${\theta_r}^*$ and Ω^* are the references of the rotor position and speed, respectively.

The standard SMC concept involves two core phases: the sliding motion, where an equivalent input $u_{eq}(t)$ sustains the state on the predefined manifold ($\mathcal{S} = 0$ and $\dot{\mathcal{S}} = 0$), and the reaching phase, driven by a switching input $u_s(t)$ that compels the trajectory to attain the surface. This produces a combined control vector:

$$\begin{bmatrix} u_{eq}(t) & u_s(t) \end{bmatrix}^t = \begin{bmatrix} {i^*}_{q,eq} & {i^*}_{q,s} \end{bmatrix}^t \tag{7}$$

The standard sliding mode control scheme can be designed as follows (Figure 5):

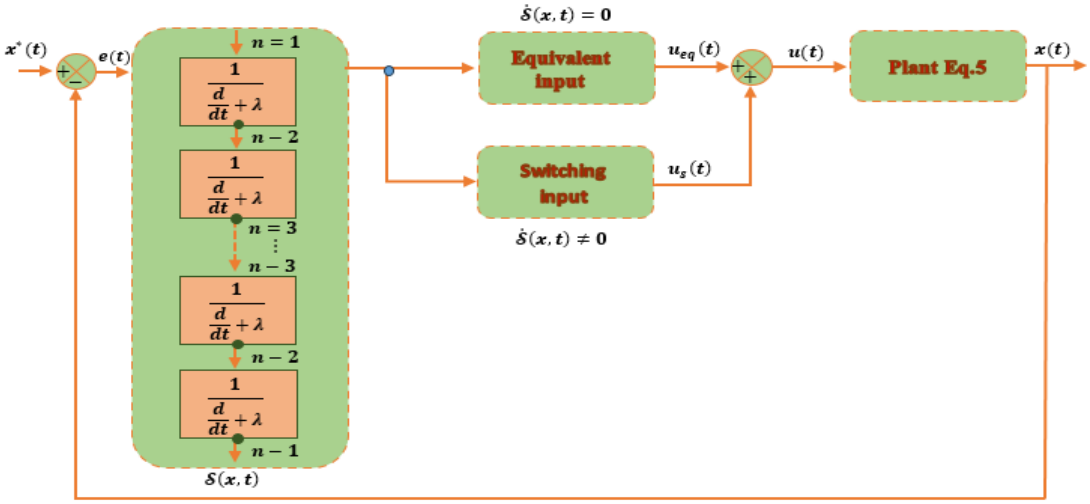

Figure 5. Standard Scheme of Sliding Mode Control.

Unlike the classical method, the terminal sliding mode introduces a nonlinear manifold to assure finite-time convergence of state errors. The chosen terminal surface takes the form [13,14,27]:

$$\sigma_1 = \dot{\mathcal{S}}_1 + \beta_t \mathcal{S}_1^{\frac{q_t}{p_t}} = \mathcal{S}_2 + \beta_t \mathcal{S}_1^{\frac{q_t}{p_t}} \tag{8}$$

with

$$\sigma_2 = \dot{\sigma}_1 = \dot{\mathcal{S}}_2 + \left(\beta_t \mathcal{S}_1^{\frac{q_t}{p_t}}\right)' = \mathcal{S}_3 + \beta_t \frac{q_2}{p_2} \mathcal{S}_2 \mathcal{S}_1^{\left(\frac{q_t}{p_t} - 1\right)} \tag{9}$$

where β_t, q_t, and p_t are design constants chosen to ensure nonlinearity in the TSMC motion and enforce rapid settling. The corresponding control rule (TSMC) incorporates an equivalent component together with a switching correction term ($u_{s,t}$) expressed as

$$u_{s-TSMC} = k_t sign(\mathcal{S}_2) \tag{10}$$

The control law based on this strategy can be calculated as follows:

$$u_{TSMC} = u_{eq-TSMC} + u_{s-TSMC} \tag{11}$$

where k_t is a positive controller parameter for the switching correction term of the TSMC.

Although this formulation improves convergence speed, it may still produce residual high-frequency oscillations, which the STA is designed to eliminate. The STA introduces a single-order correction to handle both the surface and its derivative, defined by [30,33,46]

$$\begin{cases} u_{STA} = -\lambda_s \cdot |\mathcal{S}_2|^{\rho_s} sign(\mathcal{S}_2) + w \\ \dot{w} = -b_s \cdot sign(\mathcal{S}_2) \end{cases} \tag{12}$$

with λ_s, b_s, and ρ_s set according to the robustness requirements used in the STA.

By integrating TSMC with the STA framework, this hybrid structure provides simultaneous finite-time convergence and chattering suppression. The final sliding surface for speed regulation is reformulated as:

$$\begin{cases} \sigma_2 = \dot{\sigma}_1 = \dot{\mathcal{S}}_2 + (\beta_h \mathcal{S}_1^{\frac{q_h}{p_h}})' = \mathcal{S}_3 + \beta_h \frac{q_h}{p_h} \mathcal{S}_2 \mathcal{S}_1^{(\frac{q_h}{p_h}-1)} \\ \sigma_2 = \dot{\Omega} - \frac{1}{J} T_e + \frac{1}{J} T_l + \frac{F}{J} \Omega + \beta_h \frac{q_h}{p_h} \mathcal{S}_2 \mathcal{S}_1^{(\frac{q_h}{p_h}-1)} \end{cases} \tag{13}$$

Then, the electromagnetic torque can be formulated as:

$$T_e = j\dot{\Omega}^* + T_l + F \cdot \Omega + j \cdot \beta_h \cdot \frac{q_h}{p_h} \mathcal{S}_2 \mathcal{S}_1^{(\frac{q_h}{p_h}-1)} \tag{14}$$

So, the equivalent law of the speed loop controlled by the HOT-STA-SMC is designed as follows:

$$i^*_{q,eq} = \frac{2}{3p\psi_f} T_e \tag{15}$$

To maintain smooth behavior near the sliding surface, the discontinuous sign function is replaced with a smooth hyperbolic tangent function, and the conventional single-order STA (SO-STA) is extended to a new high-order STA (HO-STA), resulting in the following switching law:

$$\begin{cases} i^*_{q,s} = -\lambda_h \cdot |\sigma_1|^{\rho_h} tgh(\sigma_1) + w_h \\ \dot{w}_h = -b_h \cdot tgh(\sigma_1) \end{cases} \tag{16}$$

and the complete current reference for the vector control is defined by:

$$i^*_q = \frac{2}{3p\psi_f} \left(j\dot{\Omega}^* + T_l + F \cdot \Omega + j \cdot \beta_h \cdot \frac{q_h}{p_h} \mathcal{S}_2 \mathcal{S}_1^{(\frac{q_h}{p_h}-1)} \right) - \lambda_h \cdot |\sigma_1|^{\rho_h} tgh(\sigma_1) + w_h \tag{17}$$

where β_h, q_h, p_h, λ_h, b_h, and ρ_h represent the novel hybrid controller parameters employed in the HOT-STA-SMC.

The control parameters of the hybrid law (β_h, q_h, p_h, λ_h, b_h, and ρ_h) are initialized based on theoretical bounds from the high-order sliding-mode stability analysis and then refined through sensitivity simulations to balance convergence speed and chattering suppression requirements of the STA and TSMC components, following established high-order sliding mode tuning procedures. Specifically, the gains associated with the STA terms are selected to satisfy the finite time convergence conditions, while the TSMC exponents and gains are chosen to ensure robustness against modeling uncertainties and disturbance rejection.

Therefore, $\beta_h > 0$; q_h, p_h are positive odd integers; $q_h > p_h$ (where $1 < \frac{q_h}{p_h} < 2$); λ_h, $b_h > 0$; and $0 < \rho_h < 0.5$.

By combining the improved convergence of terminal sliding surfaces with the robust noise immunity of the HO-STA law, this hybrid solution (HOT-STA-SMC) achieves precise, smooth, and reliable PMSM speed tracking, effectively tackling chattering and guaranteeing finite-time performance under practical uncertainties, disturbances or any perturbations.

Although the proposed HOT-STA-SMC incorporates nonlinear functions such as power terms and hyperbolic tangent functions, the resulting computational burden remains compatible with real-time implementation. These nonlinear operations are evaluated once per sampling period and can be efficiently realized using standard techniques such as lookup tables or polynomial approximations, which are commonly adopted in digital motor drive systems. With typical sampling times employed in PMSM control (on the order of 50–100 μs), the proposed control strategy is feasible for implementation on modern digital control platforms.

3.2. Sensorless Observer Design Based on MRAS for PMSM Speed Estimation

To eliminate mechanical sensors and enhance system dependability, a MRAS is widely employed for sensorless speed estimation in PMSMs. This adaptive approach exploits the machine's inherent electromechanical relationships to estimate rotor speed in real time while preserving robust performance under parameter variations and external disturbances. The core idea of MRAS is to utilize two parallel models: a reference model that reflects the true machine behavior, and an adjustable model whose output is adaptively tuned to match the reference. The convergence between the two provides the estimated rotor speed without the need for direct mechanical measurement. In this scheme, the reference model determines the stator current components along the direct and quadrature axes (i_d and i_q) based on direct current measurements projected through the Park transformation. In parallel, the adjustable model reconstructs these same current components ($\hat{i}_d$ and $\hat{i}_q$) using both measured stator currents and voltages (u_d and u_q), together with an internal estimate of the rotor speed. The difference between the reference and adjustable models forms the adaptation signal that continuously drives the estimated speed to align with the true rotor dynamics. This adaptation is typically handled by a simple but effective PI compensator that ensures stable convergence. Figure 6 presents the framework of the MRAS-based sensorless speed estimation scheme for the PMSM [5,6,10,60].

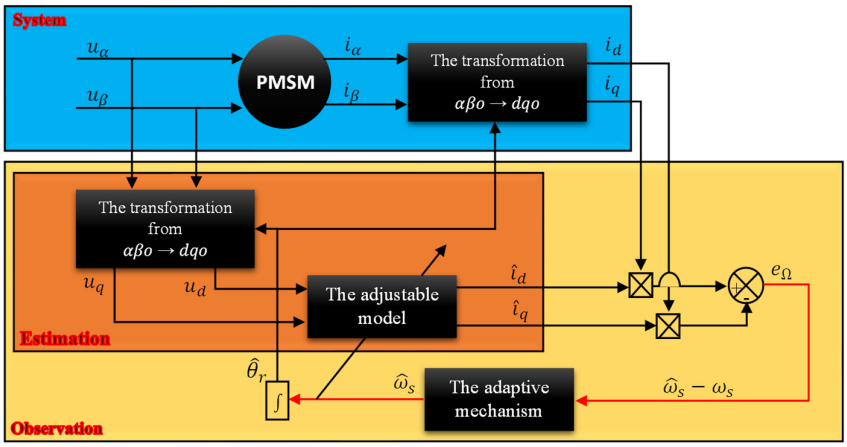

Figure 6. MRAS-based principle for PMSM sensorless speed estimation.

A critical aspect of this estimation strategy is the choice of a reference frame synchronized with the rotor. The transformation relies on the estimated rotor position, ensuring correct projection between the stator stationary frame (α-β) and the rotating (d-q) frame. A Clarke transformation is first applied to derive the stator quantities in the stationary two-axis frame, which are then mapped to the rotor-aligned coordinates via the Park transformation using the estimated rotor angle [5,6,10,60].

The PMSM's dynamic behavior in the rotor reference frame can be described by the state-space model:

$$\frac{d}{dt}\begin{bmatrix} i_d & i_q \end{bmatrix}^T = \begin{bmatrix} -R_s/L_d & \omega_s \\ -\omega_s & -R_s/L_q \end{bmatrix} \cdot \begin{bmatrix} i_d & i_q \end{bmatrix}^T + \begin{bmatrix} 1/L_d & 0 \\ 0 & 1/L_q \end{bmatrix} \cdot \begin{bmatrix} u_d & u_q \end{bmatrix}^T + \begin{bmatrix} 0 \\ -\omega_s \frac{\psi_f}{L_q} \end{bmatrix} \quad (18)$$

In contrast, the stator currents in the rotating frame can be reconstructed from the stationary frame currents (i_α, i_β) using

$$\begin{cases} i_d = i_\alpha \cos\widehat{\theta}_r + i_\beta \sin\widehat{\theta}_r \\ i_q = -i_\alpha \sin\widehat{\theta}_r + i_\beta \cos\widehat{\theta}_r \end{cases} \quad (19)$$

where $\widehat{\theta}_r$ is the estimated electrical rotor position. This transformation serves as the speed-independent reference model. In parallel, the adjustable model follows a similar structure but depends on the estimated speed $\widehat{\omega}_s$:

$$\frac{d}{dt}\begin{bmatrix} \hat{i}_d & \hat{i}_q \end{bmatrix}^T = \begin{bmatrix} -R_s/L_d & \widehat{\omega}_s \\ -\widehat{\omega}_s & -R_s/L_q \end{bmatrix} \cdot \begin{bmatrix} \hat{i}_d & \hat{i}_q \end{bmatrix}^T + \begin{bmatrix} 1/L_d & 0 \\ 0 & 1/L_q \end{bmatrix} \cdot \begin{bmatrix} u_d & u_q \end{bmatrix}^T + \begin{bmatrix} 0 \\ -\widehat{\omega}_s \frac{\psi_f}{L_q} \end{bmatrix} \quad (20)$$

The difference between the two current estimations represents the model mismatch:

$$\begin{cases} e_d = i_d - \hat{i}_d \\ e_q = i_q - \hat{i}_q \end{cases} \quad (21)$$

The evolution of this estimation error is governed by

$$\begin{cases} \frac{de_d}{dt} = -\frac{R_s}{L_d} e_d + \frac{L_q}{L_d} \widehat{\omega}_s \cdot e_q + \frac{L_q}{L_d} i_q (\omega_s - \widehat{\omega}_s) \\ \frac{de_q}{dt} = -\frac{R_s}{L_q} e_q - \frac{L_d}{L_q} \widehat{\omega}_s \cdot e_d - \frac{L_d}{L_q} i_d (\omega_s - \widehat{\omega}_s) \end{cases} - \frac{\psi_f}{L_q}(\omega_s - \widehat{\omega}_s) \quad (22)$$

This can be compactly expressed in matrix form as

$$\frac{d}{dt}\begin{bmatrix} e_d \\ e_q \end{bmatrix} = \begin{bmatrix} -\frac{R_s}{L_d} & \frac{L_q}{L_d}\widehat{\omega}_s \\ -\frac{L_d}{L_q}\widehat{\omega}_s & -\frac{R_s}{L_q} \end{bmatrix} \begin{bmatrix} e_d \\ e_q \end{bmatrix} + \begin{bmatrix} \frac{L_q}{L_d} i_q \\ -\frac{L_d}{L_q} i_d - \frac{\psi_f}{L_q} \end{bmatrix} (\omega_s - \widehat{\omega}_s) \quad (23)$$

This representation highlights how the speed estimation error directly influences the current estimation error. In the closed-loop MRAS, the dynamic error system can be represented as

$$s[e] = [A][e] + [L] \quad (24)$$

where $[A]$ is the system matrix, $[L]$ denotes the speed adaptation signal, and s is the Laplace operator. This adaptive mechanism forms a feedback loop that continuously drives the adjustable model to match the reference. The complete observer can be depicted as a nonlinear feedback system, comprising a linear block with transfer matrix $H(s) = (s[I] - [A])^{-1}$ and a nonlinear adaptation loop ensuring convergence. For the estimation loop to guarantee global stability, the closed-loop transfer matrix must be strictly positive real, ensuring that all poles lie in the left half-plane. As shown in Figure 7, the nonlinear counter-reaction system is formulated by Equations (23) and (24) [5,6,10,11,60].

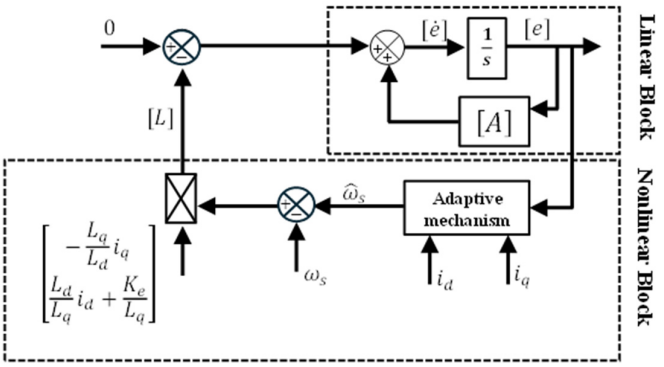

Figure 7. MRAS configured as a closed-loop system.

3.3. Stability Analysis of the Proposed Sensorless Control Scheme

The stability of the proposed sensorless control scheme is rigorously demonstrated by jointly analyzing both the closed-loop hybrid control law (HOT-STA-SMC) and the MRAS-based observer. This ensures that the overall system remains robust and convergent under operating uncertainties and external disturbances. The Lyapunov direct method is employed for the control law proof, while Popov's hyperstability criterion supports the observer stability demonstration.

To establish the closed-loop system's stability under the designed hybrid control (HOT-STA-SMC), a Lyapunov candidate function is selected as follows [7,14–16]:

$$V_\sigma = \frac{1}{2}{\sigma_1}^2 \tag{25}$$

This function is positive definite, and the system is stable if its time derivative is negative definite. Differentiating yields

$$\dot{V}_\sigma = \sigma_1 \cdot \dot{\sigma}_1 = \sigma_1 \cdot \sigma_2 \tag{26}$$

The surface derivative is governed by the PMSM dynamics combined with the control law and can be expressed as

$$\sigma_2 = -\frac{1}{J}(T_e - T_l - F \cdot \Omega) + \beta_h \frac{q_h}{p_h} \mathcal{S}_2 \mathcal{S}_1^{\left(\frac{q_h}{p_h} - 1\right)} \tag{27}$$

Substituting the electromagnetic torque expression and the relevant dynamic equations gives

$$\sigma_2 = -\frac{1}{J}\left[\left(\frac{2}{3} p \cdot \psi_f\right) \cdot {i^*}_q - T_l - F \cdot \Omega\right] + \beta_h \frac{q_h}{p_h} \mathcal{S}_2 \mathcal{S}_1^{\left(\frac{q_h}{p_h} - 1\right)} \tag{28}$$

By substituting Equation (17) into Equation (28), the following expression is obtained:

$$\sigma_2 = -\frac{1}{J} \cdot \left(\frac{2}{3} p \cdot \psi_f\right) \cdot {i^*}_{q,s} \tag{29}$$

The HO-STA gains are selected to ensure that the resulting derivative remains strictly negative definite, satisfying the condition

$$\lambda_h, b_h < 0 \tag{30}$$

which guarantees the asymptotic convergence of the tracking error to zero despite parameter variations and load disturbances.

For the inner current loop, the ERL-SMC parameters ($K_{d,h}{}'$), ($K_{d,h}$), ($K_{q,h}{}'$), and ($K_{q,h}$) are selected to enforce fast convergence of the (d)- and (q)-axis currents while maintaining robustness against parameter uncertainties and inverter nonlinearities. These gains are tuned through a coordinated tuning process that considers the interaction between the speed control loop, the sensorless observer, and the current control loop. Specifically, the reaching law gains are first initialized to ensure sufficient attraction speed toward the sliding surface, then refined through synchronized closed-loop simulations to balance current tracking accuracy, ripple suppression, and overall system stability. This global tuning strategy ensures coherent dynamic behavior across all controlled subsystems, leading to stable operation and precise current tracking under varying speed and load conditions.

Therefore, the gains multiplying the sliding surfaces of the d–q currents are chosen to be sufficiently small ($0 < K_{d,h}{}', K_{q,h}{}' < 1$), whereas the gains multiplying the hyperbolic tangent functions are selected to be relatively large, satisfying the condition ($K_{p\widehat{\omega}_s} < K_{d,h}$, $K_{q,h} < K_{i\widehat{\omega}_s}$). This selection guarantees fast current convergence, smooth control action, and stable operation of the overall sensorless PMSM drive.

In parallel, the stability of the rotor speed estimation using the MRAS observer is verified by applying Popov's hyperstability criterion. According to this approach, the feedback loop satisfies hyperstability if the following inequality holds [7,10,60]:

$$\int_0^{t_1} e^t L \, dt \geq -\chi^2 \qquad \text{For} \quad t_1 \geq 0 \tag{31}$$

where χ is a positive constant, and $e = \begin{bmatrix} i_d & i_q \end{bmatrix}^t$ is the vector of estimation errors.

The estimated rotor speed is formulated by

$$\widehat{\omega}_s = A_2(e) + \int_0^t A_1(e) dt \tag{32}$$

with the nonlinear functions $A_1(e)$ and $A_2(e)$ expressed as

$$\begin{cases} A_1 = K_1 \left[\frac{L_q}{L_d} e_d i_q - \frac{L_d}{L_q} e_q i_d - \frac{\psi_f}{L_q} e_q \right] \\ A_2 = K_2 \left[\frac{L_q}{L_d} e_d i_q - \frac{L_d}{L_q} e_q i_d - \frac{K_e}{L_q} e_q \right] \end{cases} \tag{33}$$

where K_1 and K_2 are positive adaptation gains. This formulation ensures that the estimated speed responds adaptively to the observed error dynamics. Popov's inequality for the MRAS structure becomes

$$\int_0^{t_0} \left\{ \left[e_d \left(\frac{L_q}{L_d} i_q \right) \right] - \left[\left[e_q \left(\frac{L_d}{L_q} i_d + \frac{K_e}{L_q} \right) \right] \right] \right\} \int_0^{t_0} \left[\omega_s - A_2([e]) - \int_0^{t_0} A_1(e) d \right] dt \geq -\gamma_0^2 \tag{34}$$

demonstrating that the observer loop remains stable and convergent. To enhance the estimation accuracy and dynamic response, a PI regulator structure is introduced, resulting in the following estimate for the rotor speed:

$$\widehat{\omega}_s = K_{i\omega_s} \int_0^t \left(\frac{L_q}{L_d} e_d i_q - \frac{L_d}{L_q} e_q i_d - \frac{\psi_f}{L_q} e_{q.} \right) dt + K_{p\omega_s} \cdot \left(\frac{L_q}{L_d} e_d i_q - \frac{L_d}{L_q} e_q i_d - \frac{\psi_f}{L_q} e_q \right) + \widehat{\omega}_s(0) \tag{35}$$

Here, $K_{i\omega_e}$ and $K_{p\omega_e}$ denote the integral and proportional gains of the PI regulator, which are employed to minimize the discrepancy between the actual rotor speed and its estimated value.

The estimated rotor electrical position is obtained through integration, as follows:

$$\widehat{\theta}_r = \int_0^t \widehat{\omega}_s dt + \theta_{e0} \tag{36}$$

In this expression, θ_{e0} defines the initial value of the estimated rotor electrical angle. To validate the dynamic response behavior, the error variation is described by

$$\Delta e(t) = e(t) - e(t - \Delta T) \tag{37}$$

where ΔT is the observation interval. The transfer function relating the deviation of the estimation error to the speed estimate is derived as:

$$G_{p\_\widehat{\omega}_s} = \frac{K_L^2(s + T_d) + K_L i_q \omega_s}{\left[(s + T_d)(s + T_q) + \omega_s^2\right]} \tag{38}$$

where $K_L = \frac{\psi_f}{L_q}$; $T_d = \frac{R_s}{L_d}$ and $T_q = \frac{R_s}{L_q}$ and the closed-loop response function is:

$$\frac{\widehat{\omega}_e}{\Delta\widehat{\omega}_e} = G_{p\_\widehat{\omega}_e}\left(\frac{K_{p\widehat{\omega}_s} + K_{i\widehat{\omega}_s}}{p}\right) \tag{39}$$

By satisfying Popov's criterion under the chosen regulator gains, the observer guarantees reliable real-time estimation of rotor speed and position. Together, the Lyapunov-based control stability and the hyper-stable observer form a robust and unified sensorless control scheme for the PMSM drive, ensuring consistent dynamic behavior and precise tracking performance across the entire operating range [10,60]. The proportional and integral gains are tuned to guarantee positive realness of the associated transfer function and fast convergence of the estimated speed error ($\Delta\widehat{\omega}_e$). These gains are adjusted to achieve a compromise between rapid estimation dynamics and noise sensitivity.

To enhance the practical applicability and reproducibility of the proposed sensorless control scheme, a systematic parameter tuning procedure is adopted. The tuning process is performed in a hierarchical and coordinated manner, starting from the PMSM model initialization, followed by the design of the speed-loop sliding surface, the adjustment of the novel HOT-STA-SMC gains, the tuning of the inner ERL-SMC current regulators, and finally the calibration of the MRAS observer gains under Popov's stability criterion. At each stage, stability, convergence speed, and robustness against load disturbances and parameter uncertainties are verified through closed-loop simulations. If global tracking performance and stability requirements are not satisfied, the corresponding subsystem gains are iteratively refined. The overall tuning workflow is summarized in the flowchart presented in Figure 8.

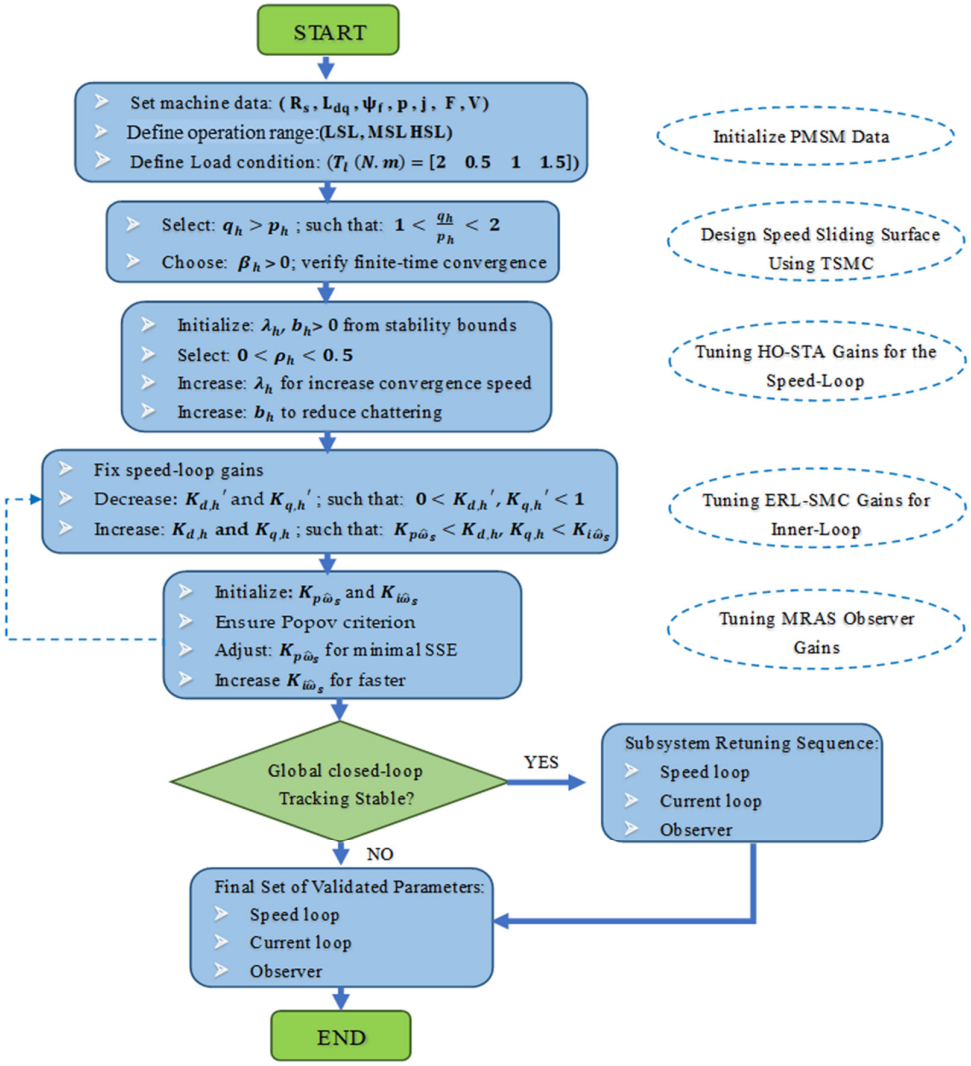

Figure 8. Systematic Parameter Tuning Procedure for the Global Closed-Loop Control.

4. Simulation Results and Discussion

To assess the performance of the proposed sensorless control strategy, simulations were conducted using the MATLAB/Simulink environment, which provides a robust platform for modeling complex dynamic systems and evaluating advanced control algorithms. The implemented simulation model reflects the complete architecture of the control system, including the machine dynamics, control blocks, and observer structure. The proposed design introduces a novel hybrid control structure for the speed regulation loop by combining the merges a terminal sliding mode controller with a high-order super-twisting approach (HOT-STA-SMC). This integration merges the finite-time convergence and precision of terminal sliding modes with the chattering reduction and strong disturbance rejection capability of single-order sliding modes. Simultaneously, the inner current loop is controlled using an ERL-SMC, which contributes to high-speed response and improved current tracking. Overall, the proposed control framework ensures fast and smooth dynamic convergence while preserving strong robustness against parameter variations, model uncertainties, and external disturbances. Additionally, the conventional MRAS-based sensorless observer has been enhanced by embedding it within the proposed control structure, resulting in improved speed estimation accuracy and greater stability across varying load conditions. This not only eliminates the need for mechanical sensors contributing to lower system cost and complexity but also reinforces the system's reliability and performance.

A detailed schematic of the overall simulation setup is provided below (see Figure 9), illustrating the interaction between the PMSM model, inverter with its control, Park transformation, the multi-layered control strategy, and the MRAS-based observer. The simulation was conducted using the system data listed in Table 1. Furthermore, the simulation results are analyzed under two representative operating scenarios. In each case, the performance of the proposed sensorless control strategy is compared against recent reference configurations, namely: STA-ERL-SMC, HOT-ERL-SMC, and ERL-PSMC-MRAS. Moreover, the robustness of the proposed control strategy has been demonstrated under parametric uncertainties. The evaluation focuses on key performance indicators such as speed tracking accuracy, current regulation, torque ripple suppression, and robustness to external load variations.

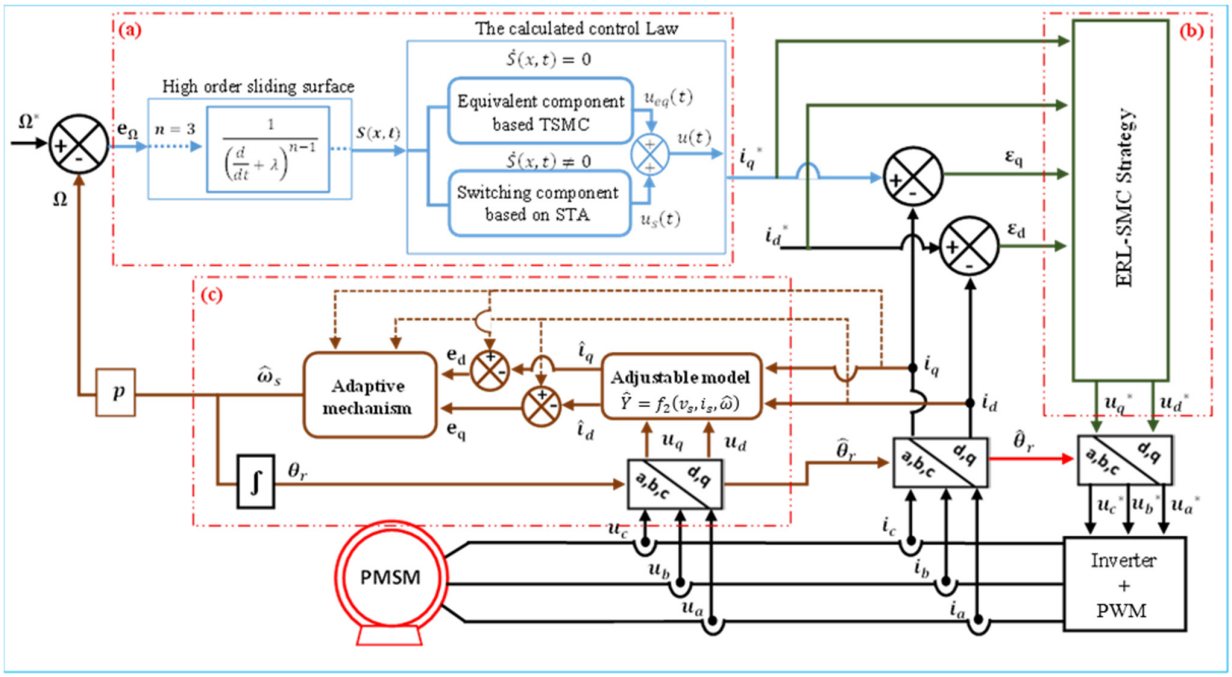

Figure 9. Simulation Scheme of the Proposed Sensorless Control Design Based on HOT-STA-SMC and MRAS.

Table 1. System data.

PMSM Parameters	Value
Stator resistance R_s	0.6 Ω
D-axis induction L_d	$1.4 \cdot 10^{-3}$ H
Q-axis induction L_q	$2.8 \cdot 10^{-3}$ H
Damping factor F	0.0014
Rotational inertia J	0.0011 kg·m^2
Magnetic flux ψ_f	0.12 Wb
Pole-pairs number p	4
DC bus voltage V	100 V

The simulation parameters are carefully selected to ensure fair and meaningful comparisons (Appendix A). For the ERL-PSMC-MRAS, the parameters are set to $k_{\Omega,\mathrm{ERL}}{}' = 0.1$, $k_{\Omega,\mathrm{ERL}} = 1$, $k_{\mathrm{d,ERL}}{}' = 0.8$, $k_{\mathrm{d,ERL}} = 50$, $k_{\mathrm{q,ERL}}{}' = 0.8$, $k_{\mathrm{q,ERL}} = 50$, $K_{p\hat{\omega}_s} = 60$, and $K_{i\hat{\omega}_s} = 9 \cdot 10^6$. The HOT-ERL-SMC implementation uses $\beta_t = 0.01$, $q_t = 11$, $p_t = 10$, $k_t = 3$, $K_{d,t}{}' = 0.008$,

$K_{d,t} = 44$, $K_{q,t}{}' = 0.008$, and $K_{q,t} = 44$. For the STA-ERL-SMC, the selected values are $\lambda_s = 0.12$, $\rho_s = 6$, $b_s = 5$, $K_{d,s}{}' = 1$, $K_{d,s} = 200$, $K_{q,s}{}' = 1$, and $K_{q,s} = 200$. Finally, in the proposed sensorless control strategy, the tuning gains are set to $\beta_h = 0.1$, $q_h = 11$, $p_h = 10$, $\lambda_h = 1.9$, $\rho_h = 0.5$, $b_h = 0.1$, $K_{p\hat{\omega}_s} = 60$, $K_{i\hat{\omega}_s} = 3{\cdot}10^6$, $K_{d,h}{}' = 0.8$, $K_{d,h} = 800$, $K_{q,h}{}' = 0.8$, and $K_{q,h} = 800$.

In the first scenario, the robustness and dynamic tracking capability of the proposed sensorless control design are evaluated under varying load torque conditions. The PMSM is subjected to a series of external torque disturbances, where the load torque changes to 2 N·m, 0.5 N·m, 1 N·m, and 1.5 N·m at time instants of 0.1 s, 0.2 s, and 0.3 s, respectively, while the speed reference remains constant at 1500 rpm. The objective of this test is to assess the system's robustness, speed regulation accuracy, and disturbance rejection capability across different load conditions, ranging from medium to high torque levels. In addition to speed dynamics, the test also examines the behavior of the electromagnetic torque and stator current responses, as these are critical indicators of the system's efficiency, control precision, and dynamic stability during load transients.

The speed result, depicted in Figure 10, present a comparative analysis between the proposed sensorless control scheme and three recent control strategies: STA-ERL-SMC, HOT-ERL-SMC, and ERL-PSMC-MRAS. The performance is evaluated based on three main criteria: robustness to load torque variation (including overshoot and undershoot behavior), speed regulation quality (rise time and steady-state error), and control efficiency during transition between various loading levels.

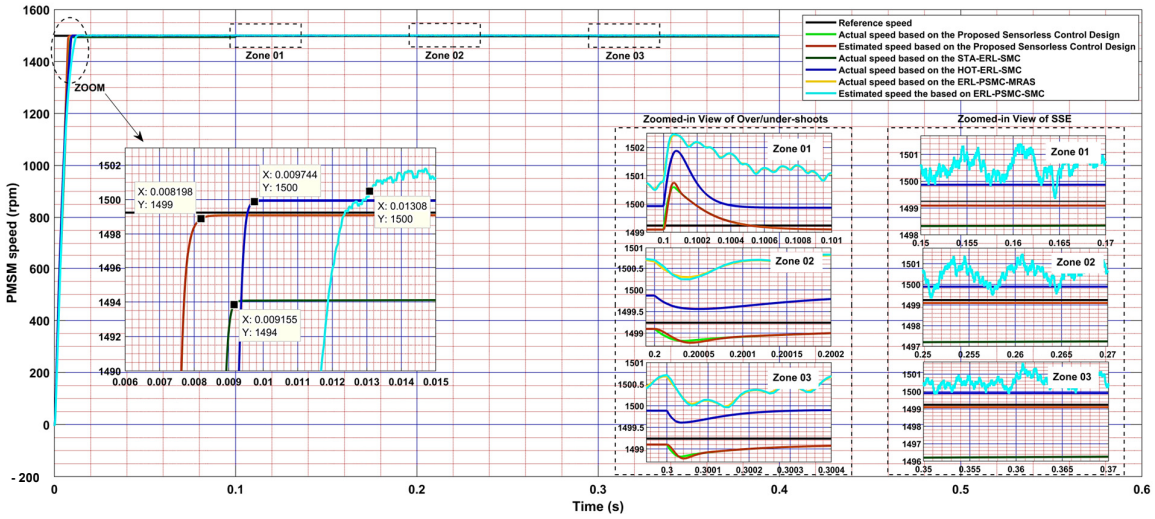

Figure 10. Speed Performance of the PMSM under the First Scenario.

From the figure, the proposed control system clearly demonstrates superior robustness. Upon the initial torque disturbance of 2 N·m at 0.1 s, the proposed method maintains a highly stable speed trajectory with negligible overshoot and undershoot. As shown in the zoomed-in view (Zone 01), the maximum undershoot does not exceed 1.8 rpm, with a fast recovery time of approximately 0.5 ms. In contrast, HOT-ERL-SMC and ERL-PSMC-MRAS exhibit deeper deviations up to 1.9 rpm and 2 rpm, respectively, along with delayed recovery times and persistent ripples. The STA-ERL-SMC configuration shows no significant overshoot peaks but suffers from a noticeable steady-state deviation when the load is applied or varied, which reduces its overall robustness compared to the proposed approach.

The proposed sensorless control achieves a rise time of approximately 8.2 ms, reaching the target speed of 1500 rpm with a fast and stable response. In the initial acceleration phase (highlighted in the left zoomed region), the speed converges rapidly and smoothly, without

any observable overshoot or oscillations. This precise behavior results from the combined action of the high-order terminal sliding mode, which ensures finite-time convergence, and the super-twisting algorithm, which effectively suppresses chattering and maintains continuous control effort. By comparison, the ERL-PSMC-MRAS method shows a clear initial overshoot of about 2 rpm and requires a longer time to settle at the reference speed. The HOT-ERL-SMC configuration does not produce a noticeable initial overshoot but shows a slower rise time compared to the STA-ERL-SMC the proposed sensorless control design, while still settling faster than the ERL-PSMC-MRAS approach. Additionally, the STA-ERL-SMC achieves a smooth initial speed profile without significant overshoot but still shows a slight deviation when conditions change, indicating slightly lower tracking quality in its response performance compared to the proposed scheme.

In terms of steady-state behavior, the proposed control scheme maintains tight regulation throughout all operating conditions, as shown in the zoomed-in SSE views (Zones 01–03). The proposed method keeps the actual and estimated speed consistently within a narrow ± 0.2 rpm band around the reference, even under higher applied loads. In comparison, the next best performance is shown by the HOT-ERL-SMC configuration, which exhibits minor SSE deviation but remains mostly within a ± 0.6 rpm range. The STA-ERL-SMC also maintains acceptable steady-state tracking but shows slightly larger SSE than the HOT-ERL-SMC, especially in Zone 03. In contrast, the ERL-PSMC-MRAS approach displays noticeable ripple and drift in all three SSE zones, with the largest fluctuations and signs of degraded synchronism when the torque steps to 2 N·m in Zone 01. Overall, the proposed design preserves stable operation with minimal steady-state oscillations, clearly outperforming the other configurations in steady-state precision.

Finally, the control efficiency under mixed torque levels (light to heavy) highlights the superiority of the proposed architecture. Its performance remains consistent and unaffected by the severity of the applied load torque. The precision in speed tracking, minimal sensitivity to load steps, and quick re-stabilization confirm the effectiveness of the proposed control law in delivering both high robustness and dynamic adaptability. In contrast, the comparative methods show degraded performance under increasing torque magnitude, indicating limitations in disturbance resilience and convergence smoothness.

Figure 11 presents the electromagnetic torque responses of the PMSM under the load conditions defined in Scenario 1. The electromagnetic torque responses were analyzed in terms of three main aspects: ripple minimization, dynamic smoothness/stability, and steady-state tracking accuracy. As observed across all time zones, the proposed control strategy yields the lowest torque ripple amplitude. Especially in Zones 01 to 04, the torque signal generated by the proposed controller (orange line) remains tightly bound with minimal oscillation around the commanded torque. In contrast, the ERL-PSMC-MRAS (light blue) response is visibly affected by significant ripple and high-frequency oscillations, particularly in the steady-state phases following each load disturbance. The HOT-ERL-SMC and STA-ERL-SMC methods show intermediate behavior, reducing some ripple but still trailing behind the proposed design. The reduced ripple in the proposed method is attributed to the continuous nature of the super-twisting component, which avoids the discontinuities typically introduced by traditional sliding mode controllers.

The proposed method demonstrates excellent smoothness and dynamic stability during the transition between different load torque levels. The response remains free from abrupt variations or chattering, and torque tracking converges without generating oscillatory transients. This is further emphasized in the zoomed-in views, where the slope and waveform trajectory of the torque profile show smoother, more controlled transitions compared to the benchmark methods. The HOT-ERL-SMC and STA-ERL-SMC show sharper transitions, while the ERL-PSMC-MRAS suffers from visible oscillations,

suggesting a lack of damping and reduced control authority during transients. The torque tracking accuracy is further validated through the evaluation of steady-state error across different zones. In each load interval, the proposed sensorless control approach aligns more precisely with the desired torque, with SSE values remaining within a very narrow band on the order of millinewton-meters (mN·m). This performance is clearly visible in Zones 01 to 04, where the proposed method consistently follows the reference with minimal offset. On the other hand, the ERL-PSMC-MRAS configuration exhibits the largest tracking error, especially under the lighter load conditions (e.g., Zone 02), with oscillation-induced deviation from the desired torque level. HOT-ERL-SMC and STA-ERL-SMC improve upon this baseline but still show non-negligible offset and noise.

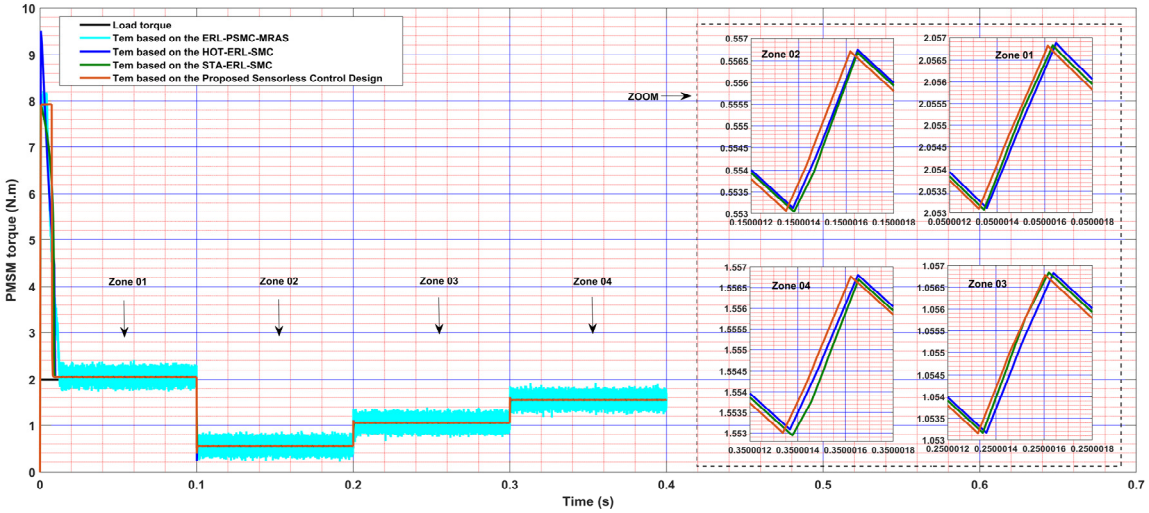

Figure 11. Electromagnetic torque Performance of the PMSM under the First Scenario.

The stator i_d and i_q current responses under dynamic load changes are presented in Figure 12. As illustrated, the proposed sensorless control design exhibits the most stable and low-ripple current behavior among all methods. In all zones, particularly during torque disturbances, both i_d and i_q currents remain well-regulated, with minimal oscillations and rapid settling. The zoomed-in regions confirm that the proposed controller ensures smooth convergence with negligible tracking error. In contrast, the ERL-PSMC-MRAS currents show high-frequency noise and notable ripple amplitude, especially in i_d. The HOT-ERL-SMC and STA-ERL-SMC schemes offer improved performance over the baseline but still display observable oscillations and less smooth transitions.

Figure 13 illustrates the stator a, b, c current waveforms under the four control configurations. The proposed sensorless control design (Figure 13d) clearly achieves superior waveform quality, with highly sinusoidal phase currents exhibiting balanced amplitude, minimal ripple, and tight containment within the desired tolerance band. Notably, the proposed method limits current overshoots during the startup transient and maintains consistent waveform symmetry and peak amplitude across all load variation intervals, highlighting its strong dynamic stability and robustness. In contrast, the ERL-PSMC-MRAS scheme (Figure 13a) suffers from pronounced ripple components and poor current shaping during and after load changes, particularly evident in the form of distorted sinusoidal traces and broader tolerance bands. The HOT-ERL-SMC (Figure 13b) offers a modest improvement in waveform quality, but still shows visible high-frequency oscillations and asymmetric peaks. The STA-ERL-SMC (Figure 13c) delivers better damping performance, yet it fails to eliminate harmonic content effectively, especially under strong torque transitions.

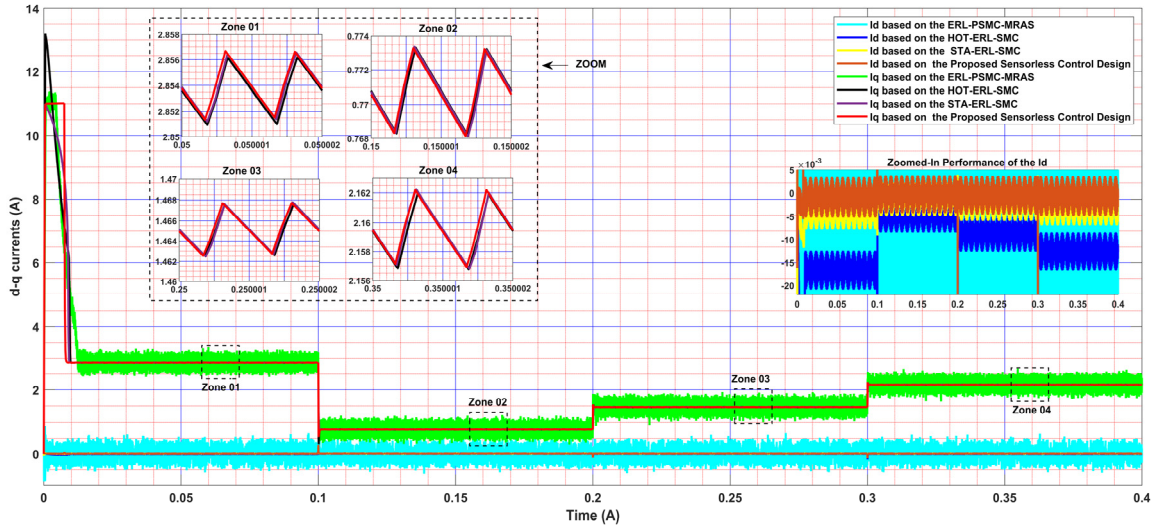

Figure 12. d-q currents Performance of the PMSM under the First Scenario.

In the second scenario, considered the most demanding test condition, the system's capability to maintain high performance is evaluated under wide speed variations spanning low (375 rpm), medium (1500 rpm), and high (4500 rpm) operating ranges while a constant load torque of 1 N·m is applied. This scenario is designed to rigorously test the proposed sensorless control design's ability to ensure precise speed tracking, stable torque response, and smooth current regulation across challenging operating points. The performance results are compared against the same reference techniques STA-ERL-SMC, HOT-ERL-SMC, and ERL-PSMC-MRAS to demonstrate the superior adaptability and robustness of the proposed hybrid design.

Figure 14 presents a comprehensive comparison of the PMSM speed regulation performance under a wide-ranging speed reference scenario, progressing from a low-speed level (LSL, 375 rpm) to a medium-speed level (MSL, 1500 rpm), and finally to a high-speed level (HSL, 4500 rpm), all under a constant load of 1 N·m. The performance of four control strategies is evaluated: ERL-PSMC-MRAS, HOT-ERL-SMC, STA-ERL-SMC, and the proposed sensorless control design. A focused analysis of the zoomed-in regions allows for a precise evaluation of the speed response characteristics for each control approach.

In terms of dynamic response, the proposed sensorless control design demonstrates consistently fast rise times across all zones, reaching approximately 2.8 ms in LSL, 5.5 ms in MSL, and 5.6 ms in HSL, giving an average rise time of 4.63 ms. This rate is notably faster than that achieved by HOT-ERL-SMC, which shows a fast rise time in the HSL zone but suffers from an initial overshoot of about 18 rpm. The ERL-PSMC-MRAS and STA-ERL-SMC also lag slightly behind, especially during the LSL transition. The STA-ERL-SMC shows a dynamic response very close to that of the proposed sensorless control design in the LSL zone but performs slightly less effectively in the MSL and HSL regions. In contrast, the ERL-PSMC-MRAS presents the lowest rise time performance among the three configurations, with initial overshoots appearing at all levels, although it performs slightly better than the HOT-ERL-SMC in the HSL zone.

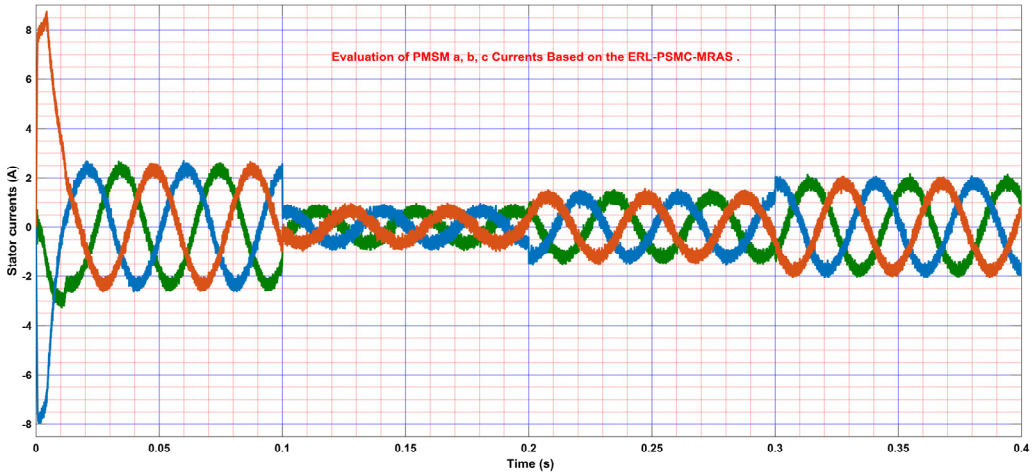

(**a**)

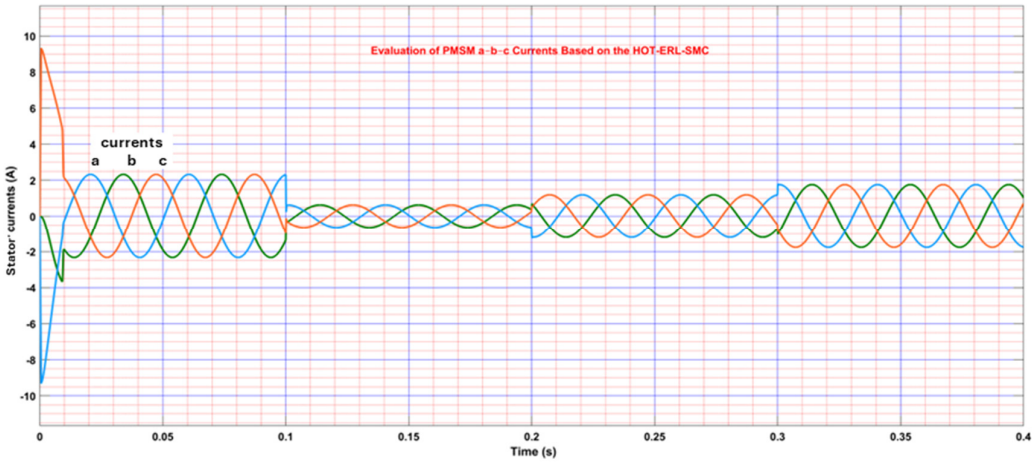

(**b**)

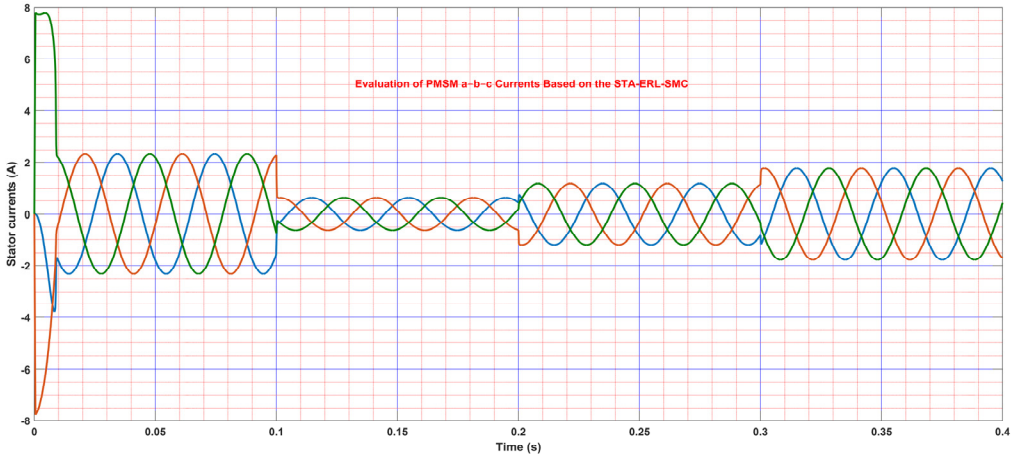

(**c**)

Figure 13. *Cont.*

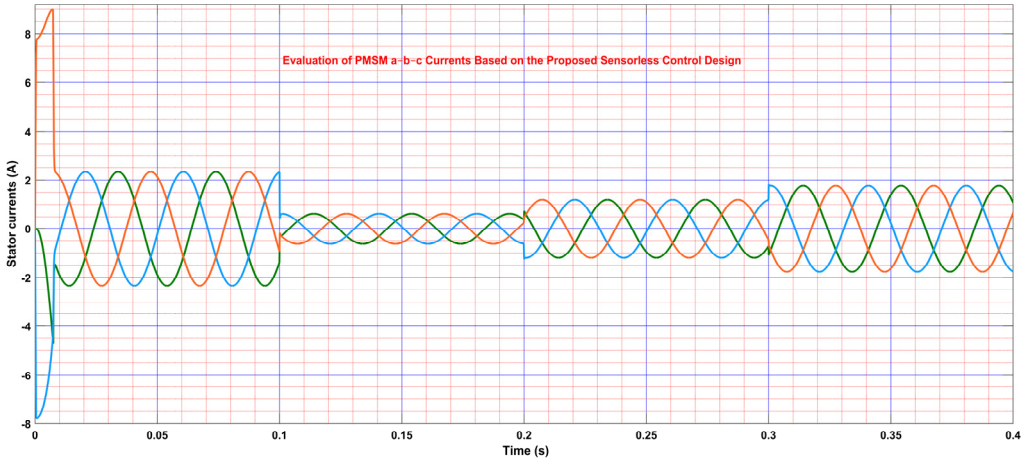

(**d**)

Figure 13. a, b, c currents Performance of the PMSM under the First Scenario; (**a**) ERL-PSMC-MRAS; (**b**) HOT-ERL-SMC; (**c**) STA-ERL-SMC; (**d**) The proposed sensorless control design.

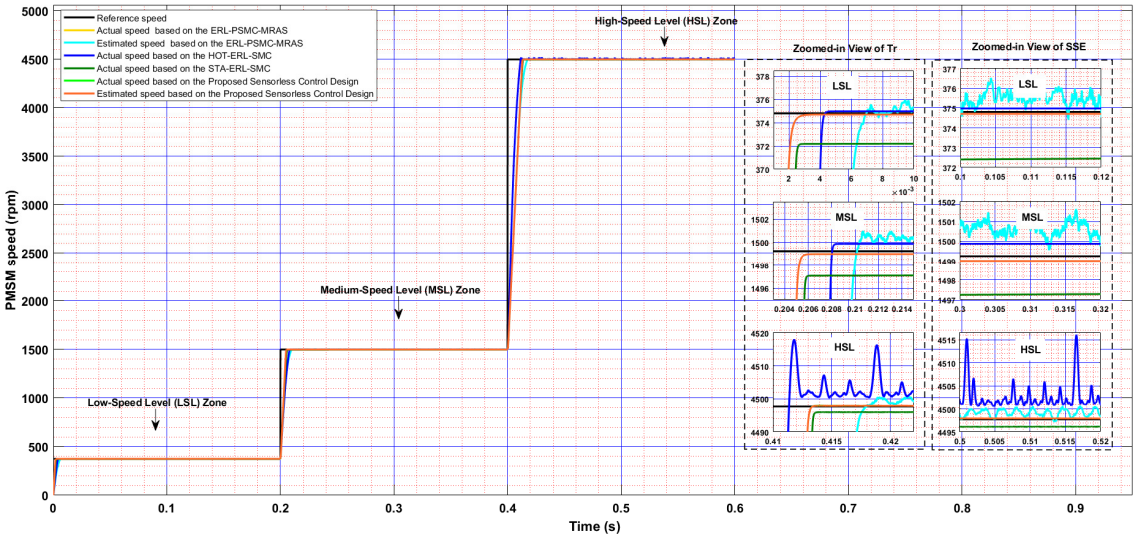

Figure 14. Speed Performance of the PMSM under the Second Scenario.

SSE analysis reveals another key strength of the proposed design. The zoomed-in SSE views across all speed levels show that the proposed method maintains an SSE within ± 0.2 rpm in LSL and MSL, and ± 0.4 rpm in HSL, resulting in an average SSE of 0.3 rpm. In contrast, the STA-ERL-SMC exhibits a relatively large SSE across all speed levels, although its output remains stable with minimal fluctuation and low-frequency effectuation, indicating consistent but offset tracking. The ERL-PSMC-MRAS, however, suffers from both high SSE and significant high-frequency oscillations throughout the LSL, MSL, and HSL zones, reflecting weaker tracking accuracy and poorer noise rejection. The HOT-ERL-SMC shows moderate performance, maintaining lower SSE compared to STA-ERL-SMC and ERL-PSMC-MRAS, especially in the LSL and MSL regions. However, its performance deteriorates significantly at HSL, where it demonstrates pronounced estimation fluctuations and instability, as clearly observed in the zoomed HSL view of Figure 14. In comparison, the proposed sensorless control design consistently outperforms the benchmark methods, achieving the lowest SSE, minimal chattering, and highly stable tracking across all speed levels, including the demanding high-speed range.

A key indicator of control stability is the overshoot behavior, and the proposed sensorless control design exhibits zero overshoot in all transitions. In contrast, HOT-ERL-SMC

shows clear overshoot in the LSL and HSL regions (as seen in the zoomed-in view of Tr), compromising the transient performance. Additionally, chattering and estimation ripple are more pronounced in the benchmark designs; particularly for HOT-ERL-SMC where speed oscillations are clearly visible during both transient and steady-state phases, as evident in the HSL view. Importantly, the proposed sensorless control design maintains smooth, stable, and ripple-free tracking under all tested speed changes, including the sharp transition from 1500 rpm to 4500 rpm. This highlights its superior adaptability and robustness in handling aggressive dynamics. The method shows minimal estimation deviation between actual and estimated speeds even under high-speed conditions, unlike the benchmark methods, where estimation lag and separation from the actual speed are noticeable especially in HOT-ERL-SMC and ERL-PSMC-MRAS. These observations confirm that the proposed sensorless control design not only delivers superior average response times and steady-state precision, but also retains high robustness and control efficiency under the harshest operating scenario.

Based on the detailed observation of Figure 15, the torque performance of the four sensorless control strategies ERL-PSMC-MRAS, HOT-ERL-SMC, STA-ERL-SMC, and the Proposed Sensorless Control Design is evaluated under three distinct speed transitions that mentioned above. In terms of torque ripple suppression, the Proposed Sensorless Control Design demonstrates superior performance across all operating zones. As seen in the zoomed views of Zones 01 and 02, it closely follows the reference load torque with minimal oscillations. Even during high dynamic transitions (Zone 03), it maintains steady torque output with minimal ripple and negligible overshoot. This contrasts with the HOT-ERL-SMC, which although acceptable at LSL and MSL, experiences significant high-frequency fluctuations and instability in HSL, as clearly illustrated in Zone 03.

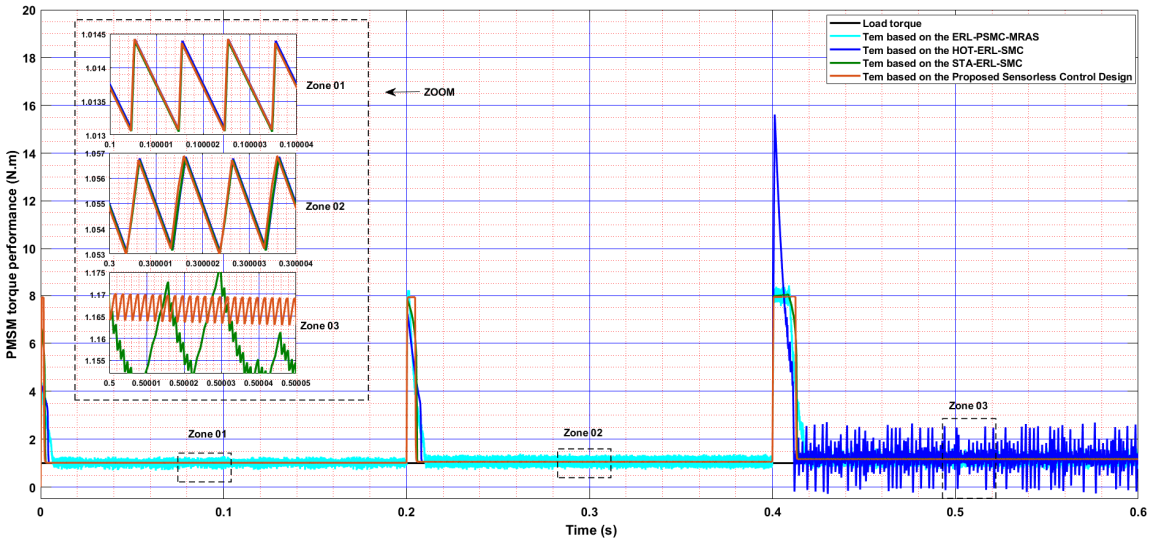

Figure 15. Electromagnetic torque Performance of the PMSM under the Second Scenario.

The STA-ERL-SMC shows slightly better ripple suppression than HOT-ERL-SMC in the HSL region; however, it suffers from visible estimation lags and lacks precision during sharp transitions. In contrast, the ERL-PSMC-MRAS control exhibits the worst performance, with persistent torque ripples even in the steady-state zones, and major disturbances during the high-speed transition. The oscillatory behavior in Zone 03 indicates poor damping and reduced robustness in torque regulation.

Regarding torque peaks during speed changes, the proposed sensorless control design exhibits the lowest transient peaks across all transition phases, highlighting its excellent damping and robust control characteristics. In the critical periods around 0.2 s and 0.4 s,

corresponding to the speed increases from LSL to MSL and from MSL to HSL, the proposed method demonstrates the most controlled and minimal torque disturbances, remaining very close to the reference with less overshoots.

In contrast, the other control strategies—particularly HOT-ERL-SMC and ERL-PSMC-MRAS—exhibit pronounced torque peaks, with HOT-ERL-SMC showing sharp spikes and sustained oscillations post-transition (as seen in Zone 03), and ERL-PSMC-MRAS displaying persistent ripples even in steady-state operation. While the STA-ERL-SMC presents slightly higher peaks during LSL and MSL transitions, its performance notably deteriorates during the HSL. As observed in Zone 03, STA-ERL-SMC displays pronounced torque ripple and instability, clearly exceeding that of the proposed sensorless control design.

Figure 16 presents the d–q axis current responses for the second scenario, including zoomed-in views that highlight the detailed behavior of the i_d and i_q components under different control strategies during the applied speed level changes described above. The zoomed view of i_d shows that the proposed sensorless control design (orange curve) keeps the i_d current very close to zero with the narrowest tolerance band (about ± 0.015 A at HSL), outperforming the ERL-PSMC-MRAS (cyan) and HOT-ERL-SMC (indigo blue), which exhibit wider bands and noticeable oscillations, especially during transitions. The STA-ERL-SMC (yellow) also maintains i_d near zero but with slightly more ripple than the proposed sensorless control design.

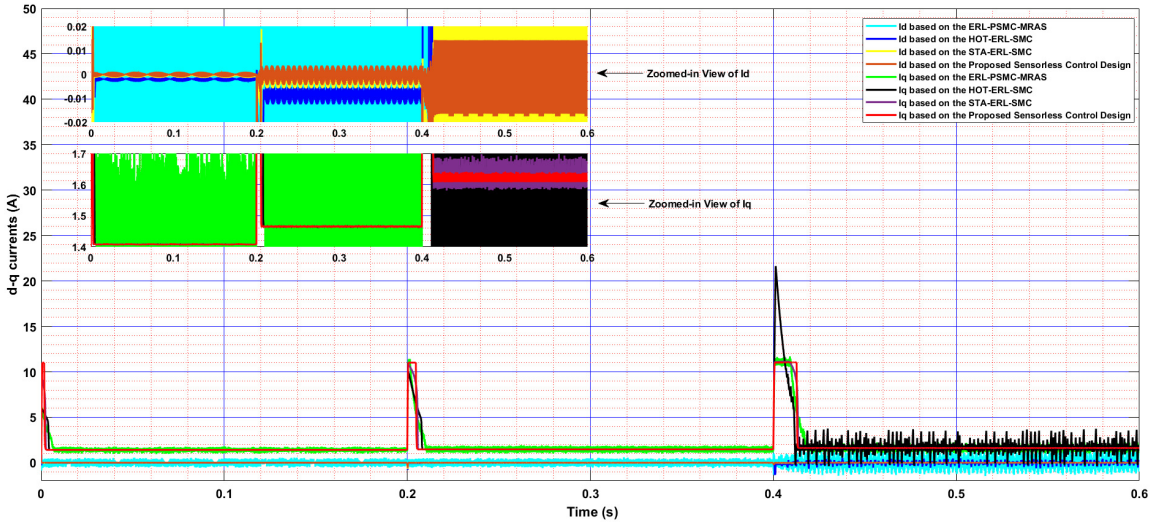

Figure 16. d-q currents Performance of the PMSM under the Second Scenario.

For the i_q component, the lower zoom confirms that the proposed method (red) achieves the most stable tracking around the desired level (~± 0.01 A at HSL) with the smoothest ripple profile. In comparison, the ERL-PSMC-MRAS (light green) exhibits the poorest performance, with the highest ripple content and the widest spread throughout the speed changes. The HOT-ERL-SMC (black) performs slightly better but still shows clear deterioration in i_q stability, especially during the HSL, where increased fluctuations appear compared to the proposed method. The STA-ERL-SMC (purple) holds i_q closer to the reference but with more residual noise than the proposed approach. Peaks during speed changes are also lowest for the proposed method, with faster settling than the others. Overall, based on tolerance band, ripple stability, and peak response, the proposed sensorless control design consistently delivers the best i_d, i_q current quality among the compared methods.

Although the proposed sensorless control design maintains superior current regulation, to further clarify the behavior observed in Figure 15—particularly the current fluctuations appearing after 0.4 s—it is necessary to analyze the operating conditions at

this instant. The fluctuations observed after 0.4 s in Figure 15 correspond to the transition toward the high-speed level (HSL = 4500 rpm), which represents the most critical operating point of the second scenario. At this stage, inverter switching effects, increased back electromotive force (back-EMF), speed-induced disturbances, inverter nonlinearities, and the amplified sensitivity to parameter mismatches collectively exacerbate high-frequency current oscillations, particularly under constant load-torque conditions. Accordingly, the residual high-frequency fluctuations observed at very high speed indicate that further performance improvements remain possible. Future work will therefore focus on enhancing inverter control through intelligent algorithms, such as artificial-intelligence-based modulation or adaptive learning strategies, as well as investigating sensorless current control schemes to further suppress switching-related disturbances. In addition, advanced filtering techniques or predictive current control formulations may be integrated to further reduce ripple and improve current smoothness under extreme operating conditions.

Under the second scenario's wide speed variations, Figure 17a (ERL-PSMC-MRAS) reveals significant current distortion, with a, b, and c phases exhibiting high ripple, irregular peak values, and poor sinusoidal shaping, particularly during transitions between speed levels. The currents frequently exceed the tolerance band, indicating weak regulation and limited dynamic stability. In Figure 17b (HOT-ERL-SMC), the abc currents exhibit good performance during the LSL and MSL, with relatively smooth waveforms, reduced ripple, and balanced peak amplitudes. However, this performance deteriorates noticeably at the HSL, where the currents show increased distortion, higher ripple content, and poorer containment within the tolerance band, indicating weakened control effectiveness under high dynamic demands. Figure 17c (STA-ERL-SMC) provides better current shaping, with improved damping and a more stable profile across the speed ranges. However, minor distortions and inconsistent containment within the tolerance band persist, especially at high speed, revealing incomplete harmonic suppression. By contrast, Figure 17d (the proposed sensorless control design) shows superior current performance, with highly sinusoidal, balanced abc waveforms tightly constrained within the tolerance band throughout all speed levels. The peak values remain consistent, ripple is minimal, and the transitions are handled smoothly, confirming the proposed sensorless control design's strong robustness and precise current regulation.

The performance of the proposed sensorless control strategy was further evaluated under extremely low-speed and zero-speed operating conditions, as illustrated in Figure 18, in order to investigate its effectiveness in the most challenging operating region of sensorless PMSM drives. Three operating cases were considered: zero-speed startup (ZSS), extremely low speed at ELS $\approx$ 20 rpm, and extremely low speed at ELS $\approx$ 50 rpm. Speed variations were introduced at 0.1 s and 0.2 s to analyze the dynamic behavior and estimation capability during low-speed transients. To further assess the effectiveness of the sensorless control schemes, the same test conditions were applied to both control strategies, allowing a direct and fair comparison between the proposed sensorless control design and the ERL-PSMC-MRAS method. The comparison focuses on the tracking performance between the estimated and actual speeds in order to evaluate the effectiveness and robustness of each control approach under extremely low-speed operation. During ZSS, where back-EMF information is inherently weak, the proposed method exhibits faster convergence toward the reference speed with significantly reduced transient deviation. The zoomed-in Tr shown in Figure 18 indicates that the proposed controller achieves smoother acceleration and reduced undershoot compared with the ERL-PSMC-MRAS approach, which presents slower estimation dynamics and larger transient oscillations.

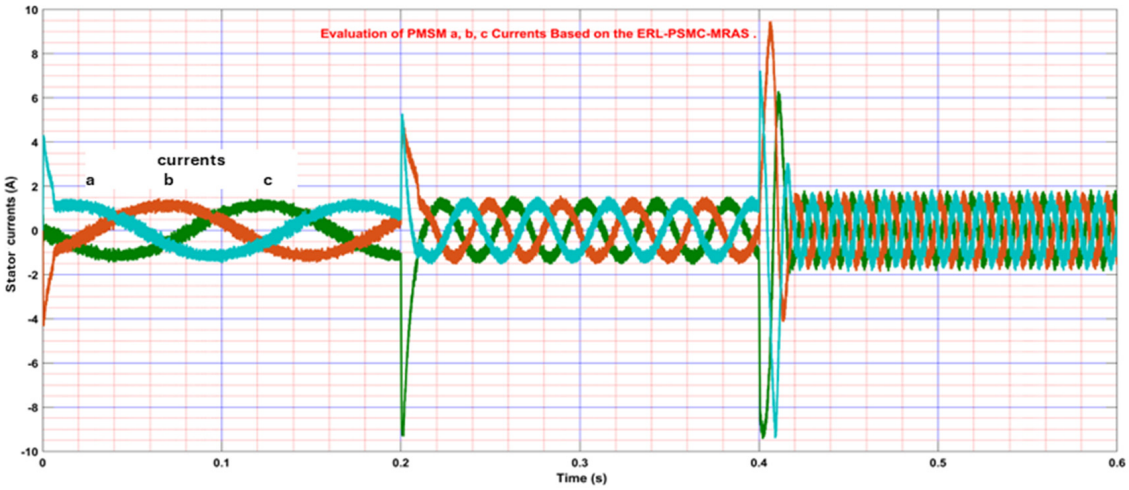

(**a**)

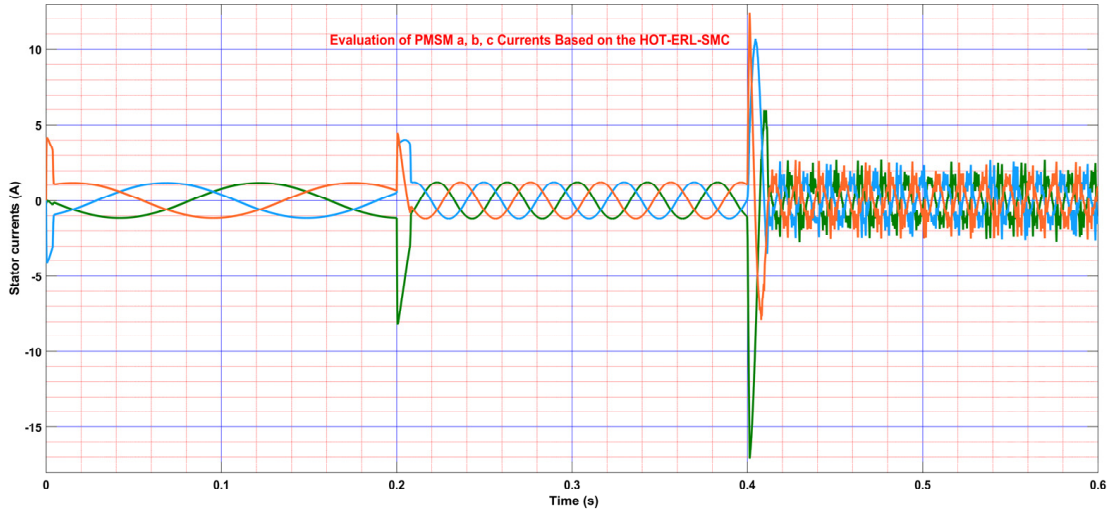

(**b**)

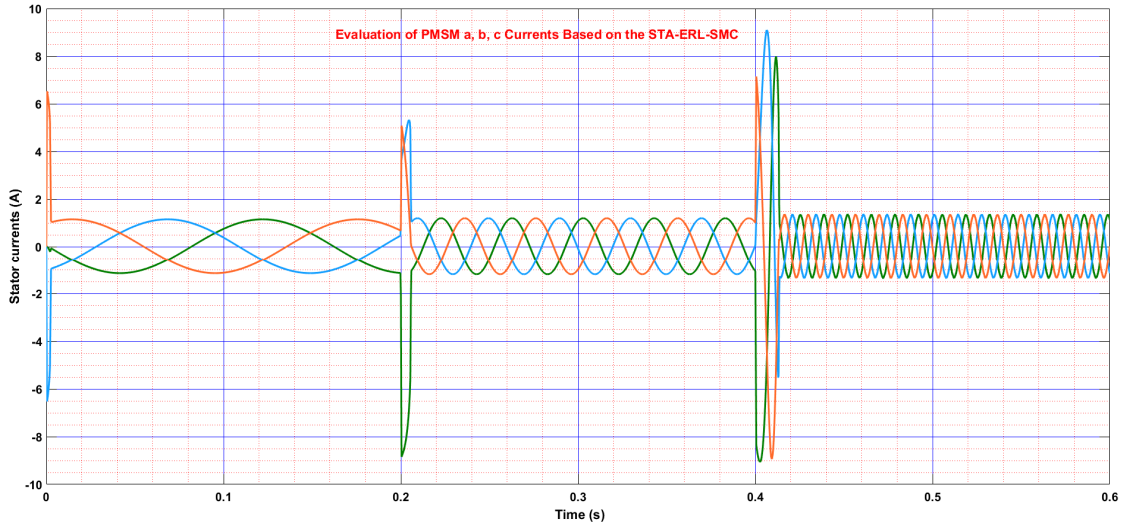

(**c**)

Figure 17. *Cont.*

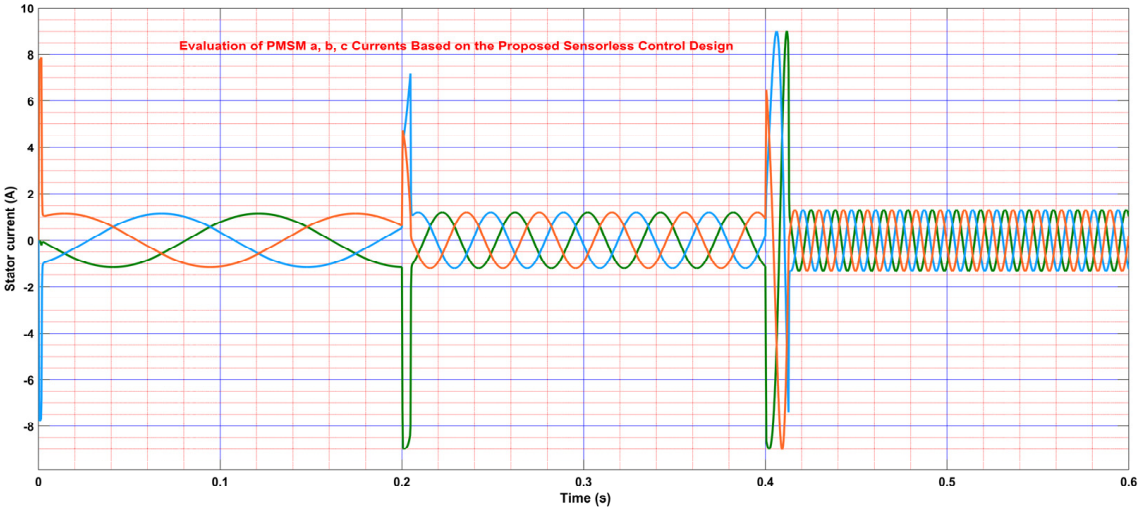

(**d**)

Figure 17. a, b, c currents Performance of the PMSM under the second Scenario; (**a**) ERL-PSMC-MRAS; (**b**) HOT-ERL-SMC; (**c**) STA-ERL-SMC; (**d**) The proposed sensorless control design.

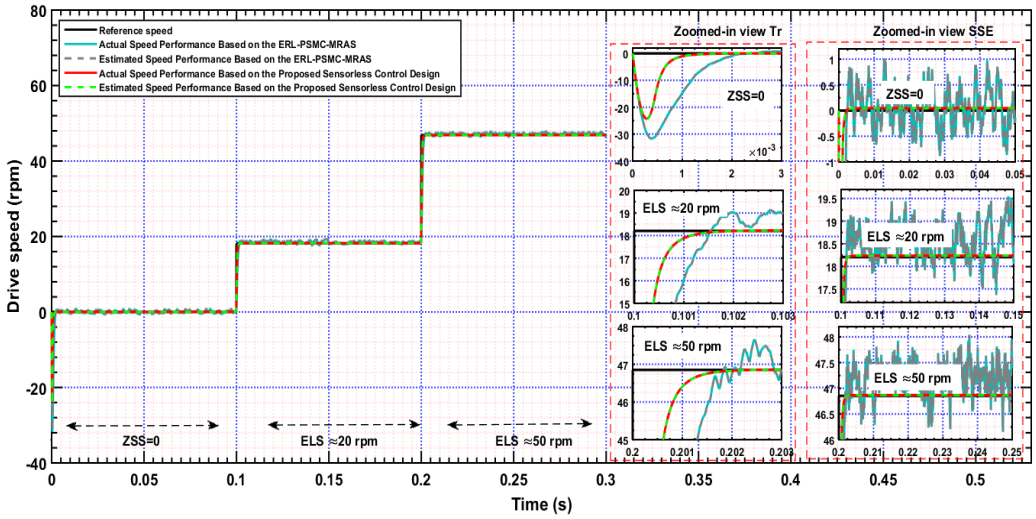

Figure 18. Speed Performance of the PMSM under the ELS and ZSS conditions.

At ELS ≈ 20 rpm, the estimated speed produced by the proposed strategy closely matches the actual speed, demonstrating accurate observation capability even in the extremely low-speed region. The SSE analysis in the zoomed view confirms a highly stable response with very small speed fluctuations. In contrast, the ERL-PSMC-MRAS technique exhibits noticeable oscillatory behavior and estimation noise, indicating reduced robustness at low-speed operation.

A similar trend is observed at ELS ≈ 50 rpm, where both controllers benefit from improved observability; however, the proposed method still provides superior performance. The transient response remains faster, and the steady-state behavior is significantly smoother, with minimal ripple between the estimated and actual speeds. The ERL-PSMC-MRAS method continues to show larger steady-state oscillations and estimation variance.

In order to demonstrate the robustness on the proposed control-observation design, the uncertainties test has been applied to change the PMSM parameters (R_s, L_d, L_q, J) to 0%, +5%, +10%, −5% and −10%, respectively, where the motor speed is stabilized at the medium operating speed of 1500 rpm and a load torque of 1 N·m is applied. Figure 19 depicts the corresponding speed responses, where the evaluation criteria are the settling time (Ts) and the steady-state error (SSE). As observed in Figure 19a, all speed responses

closely track the reference signal despite the applied parameter variations, indicating that both transient and steady-state performances are weakly affected by uncertainties. In order to detail the characteristics of the speed performance under this test, Figure 19b,c are enlargements of the T_r and SSE regions represented in Figure 19a.

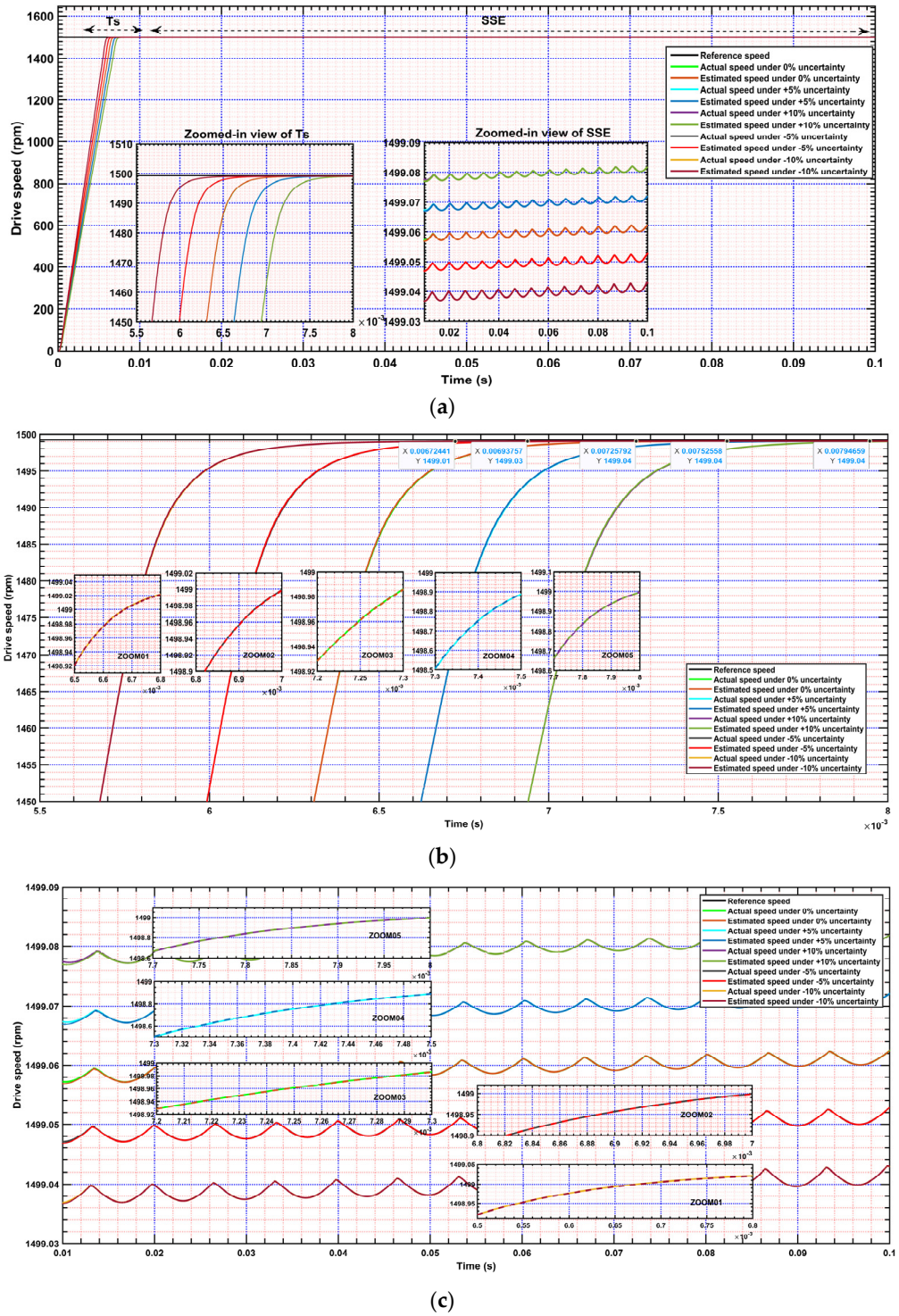

Figure 19. Speed Performance of the PMSM with the Proposed Sensorless Control Design under the uncertainties test; (**a**) SSE regions, (**b**,**c**) enlargements of the T_r.

From the zoomed-in views of the transient response (ZOOM01–ZOOM05) that represent in Figure 19b, the Ts values can be accurately identified as approximately 6.7 ms (−10%), 6.9 ms (−5%), 7.20 ms (0%), 7.5 ms (+5%), and 7.9 ms (+10%). Using these values,

the rate of change of the Ts, calculated as ([Ts(0%) + Ts(−5%) + Ts(−10%) + Ts(+5%) + Ts(+10%)]/5), is approximately 7.24 ms, confirming a limited dispersion of the transient response under parameter uncertainties.

Similarly, the steady-state behavior is analyzed using the enlarged views in Figure 19c (ZOOM01–ZOOM05), where the SSE remains tightly bounded. The steady-state error is approximately 0.21 rpm (−10%), 0.20 rpm (−5%), 0.19 rpm (0%), 0.18 rpm (+5%), and 0.17 rpm (+10%). Based on these values, the rate of change of the steady-state error (SSE), computed using the same averaging formulation, is approximately 0.19 rpm, while the variation in the speed SSE remains within 0.01 rpm, indicating very high steady-state accuracy. The small magnitude of both the rise-time and steady-state-error variations confirms that the speed performance is well preserved despite simultaneous electrical and mechanical parameter uncertainties. These results clearly demonstrate the effectiveness of the proposed control-observation design under parametric uncertainties. Tags for the two operating scenarios are outlined in Table 2.

Table 2. Comparative Evaluation of the Applied PMSM Control Configurations Across the Studied Operating Scenarios.

Performance Characteristics			ERL-PSMC-MRAS	HOT-ERL-SMC	STA-ERL-SMC	The Proposed Sensorless Control Design
Speed SSE (rpm) During speed levels		LSL	±0.6	±0.35	±2.2	±0.2
		MSL	±1	±0.6	±2	±0.2
		HSL	±1.25	±3	±1.5	±0.4
		average	0.33	1.3	0.35	0.1
Tr (ms) During speed levels		LSL	7	4.1	2.9	2.8
		MSL	10.2	8	6	5.5
		HSL	12.4	3	6.2	5.6
		average	2.7	4.45	1.65	1.4
Speed Undershoots/overshoots under disturbance (rpm)			More than 2	nearly 1.9	Big SSE	Less 1.8
Torque Ripple under speed change (N·m)		LSL	Very	±0.00075	±0.00075	±0.00075
		MSL	Very	±0.002	±0.002	±0.002
		HSL	Very Large	Very Large	±0.01	±0.0025
d-q Current Tolerance Band (A)	i_d	LSL	Very	±0.001	±0.001	±0.001
		MSL	Very	±0.005	±0.005	±0.005
		HSL	Very Large	Very Large	±0.025	±0.015
	i_q	LSL	Large	Nearly 0	Nearly 0	Nearly 0
		MSL	Large	±0.001	±0.001	±0.001
		HSL	Very Large	Very Large	±0.06	±0.01
abc Current		Quality	Poorest waveform	Weak under HSL	Good	smoothest
		Phase Balance	Heavily imbalanced	Imbalanced on the HSL	Well balanced	Perfectly balanced
		Fluctuation	Large ripple	High-frequency noise on the HSL	Minor ripple	Low ripple
Estimated Efficiency (%)			60	75	80	92
Stability			Weak at transitions	Drops at HSL	Stable	Highly stable
Robustness			Low	Degrades at HSL	High	Very High

5. Conclusions

In this work, an advanced sensorless control scheme for PMSMs has been successfully developed and validated through comprehensive simulations in MATLAB/Simulink. The proposed hybrid speed loop controller, which merges terminal sliding mode control with a HOT-STA-SMC, demonstrated remarkable capabilities in achieving finite-time convergence with minimal chattering and strong resilience to model uncertainties and external disturbances. The inner current regulation loop, designed using an ERL-SMC, further ensured

fast dynamic tracking and robust current stability under various operating conditions. By integrating an enhanced MRAS-based observer into the overall control architecture, the system achieved improved speed estimation accuracy and reliable sensorless operation without the need for physical speed sensors, thereby reducing system complexity and cost. The simulation results clearly validated the effectiveness of the proposed strategy, showing smooth electromagnetic torque response, minimized current ripples, and stable performance under load fluctuations. This work contributes a significant advancement toward the realization of high-performance, robust, and cost-efficient PMSM drive systems, with promising applicability in domains such as electric vehicles, renewable energy systems, and industrial automation. Future research may further extend this framework to experimental validation incorporating inverter nonlinearities, measurement noise, and sampling delays, ensuring real-time feasibility and practical applicability. Additionally, hybrid sensorless approaches combining MRAS observers for medium- and high-speed operation with saliency-based or high-frequency signal injection techniques for zero- and low-speed conditions could enable seamless speed estimation across the full operating range. Further studies on systematic parameter selection and tuning are also envisaged to enhance reproducibility and facilitate implementation on modern DSPs and microcontrollers. The framework could additionally be adapted for multiphase machines and fault-tolerant applications, strengthening its relevance for modern drive technologies.

Author Contributions: Conceptualization, D.K., S.B. and F.J.R.-R.; methodology, D.K., S.B. and F.J.R.-R.; software, D.K., S.B. and A.A.B.; validation, D.K., S.B., A.A.B. and F.J.R.-R.; formal analysis, D.K., S.B. and A.A.B.; investigation, D.K., S.B., A.A.B. and F.J.R.-R.; resources, D.K. and S.B.; writing—original draft preparation, D.K. and S.B.; writing—review and editing, D.K., S.B., A.A.B. and F.J.R.-R.; supervision, D.K. and F.J.R.-R. All authors have read and agreed to the published version of the manuscript.

Funding: This research received no external funding.

Data Availability Statement: Data are available from the authors upon reasonable request.

Conflicts of Interest: The authors declare no conflicts of interest.

Appendix A

For a fair comparison, the same speed reference variations applied in Section 4 are retained for LSL and MSL. For HSL, the reference speed is intentionally limited to below 3000 rpm to prevent severe performance degradation of the FOC scheme, which is highly sensitive to higher speeds. In addition, a load torque disturbance is applied, varying from 0.5 N·m to 1.5 N·m at t = 0.3 s, in order to evaluate disturbance rejection under dynamic operating conditions. Figure A1 illustrates the speed responses obtained using the FOC, ERL-PSMC, and ERL-PSMC-MRAS strategies. The FOC exhibits the slowest rise time, noticeable overshoot, and the largest steady-state speed error, particularly during speed transitions and load variation. The ERL-PSMC improves the transient response; however, residual oscillations remain. In contrast, the ERL-PSMC-MRAS achieves faster convergence with smaller overshoot and a narrower SSE band compared to the FOC and ERL-PSMC.

The electromagnetic torque responses shown in Figure A2 further emphasizes these differences. The FOC produces significant torque ripple and pronounced overshoots during speed changes and load application, reflecting its limited robustness. The ERL-PSMC reduces ripple compared to FOC but still exhibits noticeable fluctuations. The proposed ERL-PSMC-MRAS demonstrates the smoother torque profile with rapid settling, indicating enhanced disturbance rejection and improved dynamic behavior compared to the two controllers that mentioned above.

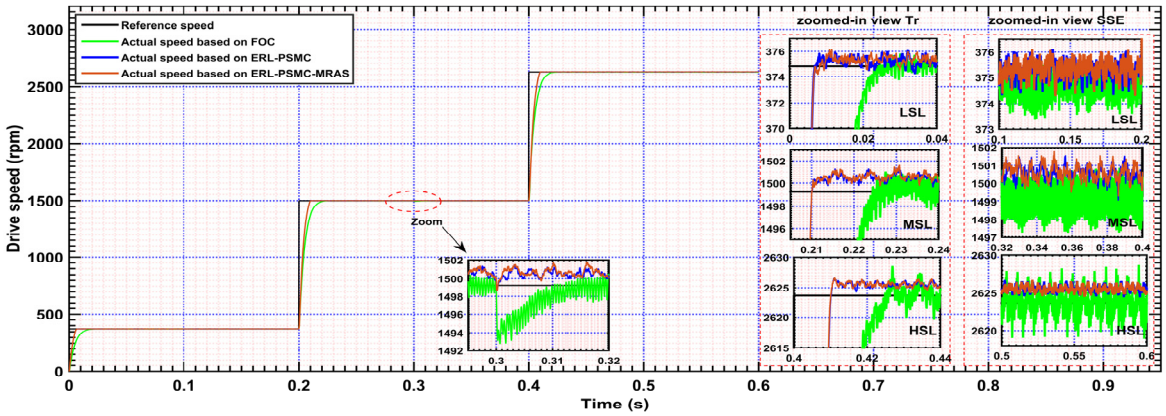

Figure A1. Speed Performance of the PMSM.

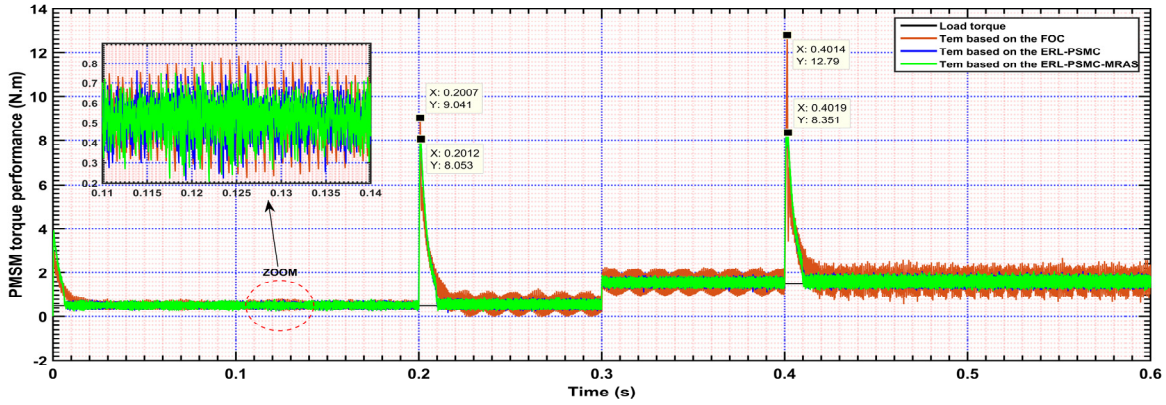

Figure A2. Torque Performance of the PMSM.

Figure A3 presents the d–q axis current responses. The FOC results in the widest tolerance bands for both (i_d) and (i_q), with clear oscillations, particularly during high-speed operation. The ERL-PSMC improves current regulation but still suffers from residual ripple. The ERL-PSMC-MRAS achieves the tighter tolerance bands than the two controllers, maintaining (i_d) close to zero and ensuring stable (i_q) tracking, which confirms precise current regulation under combined speed and load variations compared to the FOC and the ERL-PSMC.

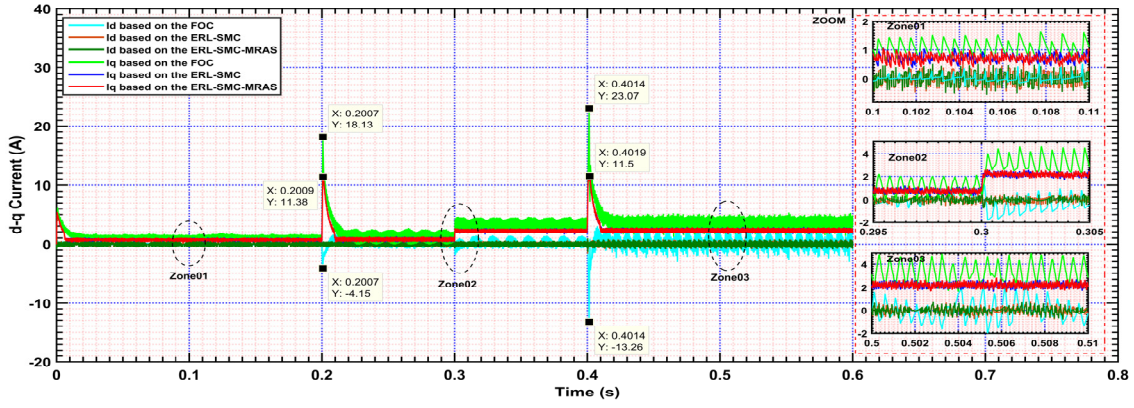

Figure A3. d-q currents Performance of the PMSM.

Finally, the three-phase stator currents depicted in Figure A4 highlight the overall current quality. The FOC (seen Figure A4a) exhibits the highest ripple content and peak amplitudes, indicating increased stress on the inverter. The ERL-PSMC FOC (seen Figure A4b)

improves waveform smoothness but retains some distortion. The ERL-PSMC-MRAS FOC (seen Figure A4c) produces better sinusoidal currents with the lower ripple and peak values compared to the two controllers.

The comparative results indicate that the conventional FOC exhibits the poorest performance under demanding operating conditions, showing the largest torque ripple, widest current tolerance bands, and the weakest dynamic response. The ERL-PSMC improves the overall performance relative to FOC; however, its dynamic behavior, robustness, and current regulation remain inferior to those of the ERL-PSMC-MRAS and the proposed sensorless control strategy. As demonstrated in Section 4, the proposed sensorless control consistently outperforms ERL-PSMC-MRAS and other recent control schemes, achieving superior transient response, enhanced disturbance rejection, reduced torque ripple, and improved steady-state accuracy. These observations collectively confirm the effectiveness and superiority of the proposed sensorless control strategy.

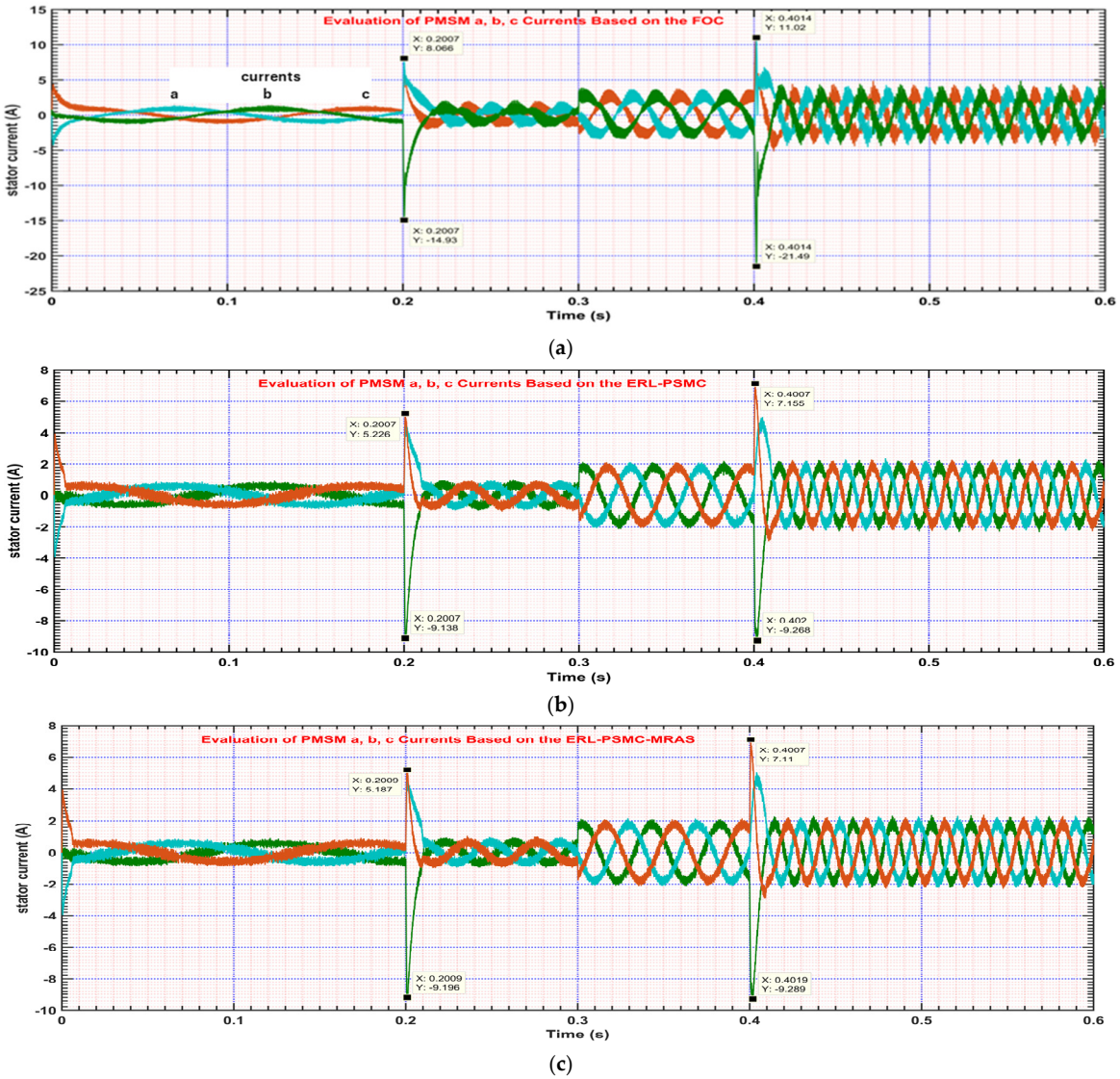

Figure A4. a, b, c currents Performance of the PMSM; (**a**) FOC; (**b**) ERL-PSMC; (**c**) ERL-PSMC-MRAS.

References

1. Li, W. Application of PMSM control in electric vehicle. *Intern. Combust. Engine Parts* **2019**, *298*, 51–52.
2. Abu-Rub, H.; Iqbal, A.; Guzinski, J. *High Performance Control of AC Drives with Matlab/Simulink*; John Wiley & Sons: Hoboken, NJ, USA, 2021.

3. Pan, Y.; Liu, X.; Zhu, Y.; Liu, B.; Li, Z. Feedforward decoupling control of interior permanent magnet synchronous motor with genetic algorithm parameter identification. *Prog. Electromagn. Res. M* **2021**, *102*, 117–126. [CrossRef]
4. Karboua, D.; Belgacem, T.; Khan, Z.H.; Kellal, C. Robust performance comparison of PMSM for flight control applications in more electric aircraft. *PLoS ONE* **2023**, *18*, e0283541. [CrossRef] [PubMed]
5. Li, Y.; Hu, H.; Shi, P. A Review of Position Sensorless Compound Control for PMSM Drives. *World Electr. Veh. J.* **2023**, *14*, 34. [CrossRef]
6. Ran, Y.; Qiao, M.; Sun, L.; Xia, Y. Review of Position Sensorless Control Technology for Permanent Magnet Synchronous Motors. *Energies* **2025**, *18*, 2302. [CrossRef]
7. Khalil, H.K. *Nonlinear Control*; Pearson: New York, NY, USA, 2015.
8. Karboua, D.; Douara, B.O.; Mebkhouta, T.; Mosaad, M.I.; Toual, B.; Ali, E.S.; Abd Elazim, S.M. Advanced Nonlinear Control Techniques for PMSM Drives: A Comprehensive Review and Comparative Analysis. *Results Eng.* **2025**, *28*, 107650. [CrossRef]
9. Teymoori, V.; Kamper, M.; Wang, R.-J.; Kennel, R. Sensorless Control of Dual Three-Phase Permanent Magnet Synchronous Machines—A Review. *Energies* **2023**, *16*, 1326. [CrossRef]
10. Landau, Y.P. *Adaptive Control: The Model Reference Approach*; M Dekker Inc.: New York, NY, USA, 1979.
11. Mebkhouta, T.; Golea, A.; Boumaraf, R.; Benchouia, T.M.; Karboua, D.; Bajaj, M.; Blazek, V. Sensorless finite set predictive current control with MRAS estimation for optimized performance of standalone DFIG in wind energy systems. *Results Eng.* **2024**, *24*, 103622. [CrossRef]
12. Janiszewski, D. Sensorless model predictive control of permanent magnet synchronous motors using an unscented kalman filter. *Energies* **2024**, *17*, 2387. [CrossRef]
13. Zaihidee, F.M.; Mekhilef, S.; Mubin, M. Robust speed control of PMSM using sliding mode control (SMC)—A review. *Energies* **2019**, *12*, 1669. [CrossRef]
14. Karboua, D.; Toual, B.; Kouzou, A.; Douara, B.; Mebkhouta, T.; Bendenidina, A.N. High-order super-twisting based terminal sliding mode control applied on three phases permanent synchronous machine. *Period. Polytech. Electr. Eng. Comput. Sci.* **2023**, *67*, 40–50. [CrossRef]
15. Utkin, V.I. Sliding mode control design principles and applications to electric drives. *IEEE Trans. Ind. Electron.* **1993**, *40*, 23–36. [CrossRef]
16. Slotine, J.J.E. *Applied Nonlinear Control*; PRENTICE-HALL: Englewood Cliffs, NJ, USA, 1991; Volume 2, pp. 1123–1131.
17. Yang, C.; Liu, W.; Song, B.; Xie, X.; Niu, S.; Chau, K.T. Signal-Injection-Based Efficient Direct-Determination of Controller Gains and Nonlinear Friction Compensation Values in SPMSM Drives. *IEEE Trans. Power Electron.* **2025**, *41*, 1627–1633. [CrossRef]
18. Karboua, D.; Mebkhouta, T.; Chouiha, Y.; Bengharbi, A.A.; Douara, B.O.; Toual, B. Enhancing Performance of Permanent Magnet Synchronous Motor Drives Through Hybrid Feedback Linearization and Sliding Mode Control. *ITEGAM-JETIA* **2024**, *10*, 178–186. [CrossRef]
19. Karboua, D.; Toual, B.; Mosaad, M.I.; Youcef, C.; Bengharbi, A.A.; Hussien, S.A. Performance enhancement of PMSM using a hybridizing of nonlinear backstepping control and an optimized linear quadratic regulator. *Energy Explor. Exploit.* **2025**, *43*, 2637–2664. [CrossRef]
20. Li, H.; Li, X.; Chen, Z.; Mao, J.; Huang, J. Model-free adaptive integral backstepping control for PMSM drive systems. *J. Power Electron.* **2019**, *19*, 1193–1202.
21. Yang, H.; Tang, J.W.; Chien, Y.R. Application of new sliding mode control in vector control of PMSM. *IEICE Electron. Express* **2022**, *19*, 20220156. [CrossRef]
22. Djaloul, K.; Belgacem, T.; Atif, I.; Youcef, C.; Toufik, M.; Ouadeh, D.B. High Order Sliding Mode Control based on a New Terminal Strategy Applied on the Speed Permanent Magnet Synchronous Machine. In Proceedings of the 2023 XIX International Scientific Technical Conference Alternating Current Electric Drives (ACED), Ekaterinburg, Russia, 23–25 May 2023; pp. 1–6. [CrossRef]
23. Zhang, Z.; Yang, X.; Wang, W.; Chen, K.; Cheung, N.C.; Pan, J. Enhanced sliding mode control for PMSM speed drive systems using a novel adaptive sliding mode reaching law based on exponential function. *IEEE Trans. Ind. Electron.* **2024**, *71*, 11978–11988. [CrossRef]
24. Li, H. A Novel Sliding-Mode-Based Control Method for Permanent Magnet Synchronous Motor Drive Systems Based on New Hyperbolic Reaching Law. *J. Electr. Eng. Technol.* **2025**, *20*, 5379–5388. [CrossRef]
25. Shang, W.; Wang, H. PMSM integral sliding mode control based on improved power exponential reaching law. *Sci. Rep.* **2025**, *15*, 21450. [CrossRef]
26. Miao, X.; Yao, W.; Ouyang, H.; Zhu, Z. Novel Composite Speed Control of Permanent Magnet Synchronous Motor Using Integral Sliding Mode Approach. *Mathematics* **2023**, *11*, 4666. [CrossRef]
27. Song, J.; Wang, Y.K.; Niu, Y.; Lam, H.K.; He, S.; Liu, H. Periodic event-triggered terminal sliding mode speed control for networked PMSM system: A GA-optimized extended state observer approach. *IEEE/ASME Trans. Mechatron.* **2022**, *27*, 4153–4164. [CrossRef]
28. Qin, G.; Wang, M.; Cao, G.; Wang, Q.; Liao, Y. PID Sliding Mode Control of PMSM Based on Improved Terminal Sliding Mode Reaching Law. *Energies* **2025**, *18*, 2661. [CrossRef]

29. Larbaoui, A.; Chaouch, D.E.; Belabbes, B.; Razkallah, M. Application of passivity-based and sliding mode control of permanent magnet synchronous motor under controlled voltage. *J. Vib. Control* **2022**, *28*, 1267–1278. [CrossRef]
30. Zhang, L.; Bai, J.; Wu, J. SPMSM sliding mode control based on the new super twisting algorithm. *Complexity* **2021**, *2021*, 9. [CrossRef]
31. Duan, J.; Wang, S.; Sun, L. Backstepping Sliding Mode Control of a Permanent Magnet Synchronous Motor Based on a Nonlinear Disturbance Observer. *Appl. Sci.* **2022**, *12*, 11225. [CrossRef]
32. Guo, Q.; Yu, H.; Yang, Q.; Gao, X.; Meng, X. Cooperative control of variable damping error port Hamiltonian and backstepping nonsingular terminal sliding mode control for manipulators driven by PMSMs. *Int. J. Robust Nonlinear Control* **2024**, *34*, 9852–9872. [CrossRef]
33. Gao, P.; Zhang, G.; Lv, X. Model-free hybrid control with intelligent proportional integral and super-twisting sliding mode control of PMSM drives. *Electronics* **2020**, *9*, 1427. [CrossRef]
34. Lu, C.; Yuan, J. Adaptive super-twisting sliding mode control of permanent magnet synchronous motor. *Complexity* **2021**, *2021*, 1957510. [CrossRef]
35. Karboua, D.; Chouiha, Y.; Douara, B.; Bouguenna, I.; Benkaihoul, S.; Toual, B. Advanced Dual-Loop Control Architecture for Superior PMSM Performance Utilizing Finite-Control-Set Model Predictive Control and Exponential Reaching Law Sliding Mode Control. *ITEGAM-JETIA* **2024**, *10*, 71–79. [CrossRef]
36. Karboua, D.; Belgacem, T.; Khan, Z.H.; Labiod, C.; Ibraheem, I.K. Toward an optimal twisting-sliding mode control of a three-phase PMSM for electric vehicles. *Adv. Mech. Eng.* **2023**, *15*, 2023. [CrossRef]
37. Chen, L.; Liu, H.; Cao, Z.; Lopes, A.M.; Yin, L.; Liu, G.; Chen, Y. Speed Control of Permanent Magnet Synchronous Motor Based on Variable Fractional-Order Fuzzy Sliding Mode Controller. *Actuators* **2025**, *14*, 38. [CrossRef]
38. Zahraoui, Y.; Zaihidee, F.M.; Kermadi, M.; Mekhilef, S.; Alhamrouni, I.; Seyedmahmoudian, M.; Stojcevski, A. Optimal tuning of fractional order sliding mode controller for PMSM speed using neural network with reinforcement learning. *Energies* **2023**, *16*, 4353. [CrossRef]
39. Zhao, Q.; Zhao, Z.; Yang, Z.; Liu, W. Speed control of sensorless PMSM drive based on EKF optimized by variable scale chaotic particle swarm optimization. *Meas. Control* **2024**, *57*, 981–991. [CrossRef]
40. Allaoui, S.; Laamari, Y.; Chafaa, K.; Saad, S. Position and Speed Estimation of PMSM Based on Extended Kalman Filter Tuned by Biogeography-Based-Optimization. *J. Eur. Systèmes Autom.* **2021**, *54*, 559–568. [CrossRef]
41. Choi, A.; Ahn, H.; Chung, Y.; You, K. Sliding Mode Control for Sensorless Speed Tracking of PMSM with Whale Optimization Algorithm and Extended Kalman Filter. *Machines* **2023**, *11*, 851. [CrossRef]
42. Meng, K.; Liu, Q.; Zhang, Z.; Wu, H.; Feng, H.; Kang, T. Sensorless HSPMSM Control of an Improved SMC and EKF Based on Immune PSO. *Appl. Sci.* **2023**, *13*, 12407. [CrossRef]
43. Tang, S.; Cao, Y.; Shi, T.; Yan, Y.; Xia, C. Online Estimation of Load Torque and Moment of Inertia Incorporating Extended Disturbance Observer with Trigger. *IEEE Trans. Power Electron.* **2025**, *40*, 5731–5742. [CrossRef]
44. Liang, J.; Wu, J.; Wang, Y.; Zhong, Z.; Bai, X. Sensorless Control for a Permanent Magnet Synchronous Motor Based on a Sliding Mode Observer. *Eng* **2024**, *5*, 1737–1751. [CrossRef]
45. Liu, W.; Luo, B.; Yang, Y.; Niu, H.; Zhang, X.; Zhou, Y.; Zeng, C. An Adaptive-Gain Sliding Mode Observer with Precise Compensation for Sensorless Control of PMSM. *Energies* **2023**, *16*, 7968. [CrossRef]
46. Wang, H.; Zhang, G.; Liu, X. Sensorless Control of Surface-Mount Permanent-Magnet Synchronous Motors Based on an Adaptive Super-Twisting Sliding Mode Observer. *Mathematics* **2024**, *12*, 2029. [CrossRef]
47. Yang, Z.; Yan, X.; Ouyang, W.; Bai, H.; Xiao, J. Multi-Parameter Fuzzy-Based Neural Network Sensorless PMSM Iterative Learning Control Algorithm for Vibration Suppression of Ship Rim-Driven Thruster. *J. Mar. Sci. Eng.* **2024**, *12*, 396. [CrossRef]
48. Chen, Y.; Li, A.; Li, H.; Yang, X.; Chen, W. Sensorless Control Method for SPMSMs Based on Improved Sliding Mode Reaching Rate. *Electronics* **2023**, *12*, 3720. [CrossRef]
49. Zhang, P.; Shi, Z.; Yu, B.; Qi, H. Research on a Sensorless ADRC Vector Control Method for a Permanent Magnet Synchronous Motor Based on the Luenberger Observer. *Processes* **2024**, *12*, 906. [CrossRef]
50. Vidlak, M.; Makys, P.; Gorel, L. A Novel Constant Power Factor Loop for Stable V/f Control of PMSM in Comparison against Sensorless FOC with Luenberger-Type Back-EMF Observer Verified by Experiments. *Appl. Sci.* **2022**, *12*, 9179. [CrossRef]
51. Gong, L.; Li, Y.; Dai, D.; Luo, W.; He, P.; Chen, J. A Sensorless Speed Estimation Method for PMSM Supported by AMBs Based on High-Frequency SquareWave Signal Injection. *Electronics* **2025**, *14*, 1644. [CrossRef]
52. Li, Z.; Inamdar, M.N.; Wang, Y. A Sensorless Control Strategy Exploiting Error Compensation for Permanent Magnet Synchronous Motor Based on High-Frequency Signal Injection. *World Electr. Veh. J.* **2025**, *16*, 261. [CrossRef]
53. Zhang, W.; Cheng, S.; Zhu, P.; Liu, Y.; Zou, J. Synchronized Carrier-Wave and High-Frequency Square-Wave Periodic Modulation Strategy for Acoustic Noise Reduction in Sensorless PMSM Drives. *Energies* **2025**, *18*, 2729. [CrossRef]
54. Yang, C.; Liu, W.; Niu, S.; Lyu, J.; Chau, K.T. Parameter-Tuning-Free Two-Step Identification of Mechanical Parameters for PMSM Drives. *IEEE Trans. Ind. Electron.* **2025**, *72*, 12378–12392. [CrossRef]

55. Zeghlache, A.; Djerioui, A.; Mekki, H.; Zeghlache, S.; Benkhoris, M.F. Robust Sensorless PMSM Control with Improved Back-EMF Observer and Adaptive Parameter Estimation. *Electronics* **2025**, *14*, 1238. [CrossRef]
56. Shao, L.; Zheng, C.; Zhang, Y.; Xie, G.; Hao, X.; Zheng, X. Research on Permanent Magnet Synchronous Motor Sensorless Control System Based on Integral Backstepping Controller and Enhanced Linear Extended State Observer. *Appl. Sci.* **2023**, *13*, 1680. [CrossRef]
57. Niu, H.; Liu, L.; Jin, D.; Liu, S. High-Tracking-Precision Sensorless Control of PMSM System Based on Fractional Order Model Reference Adaptation. *Fractal Fract.* **2023**, *7*, 21. [CrossRef]
58. Chen, A.; Chen, W.; Wan, H. PMSM Sensorless Control Based on Moving Horizon Estimation and Parameter Self-Adaptation. *Electronics* **2024**, *13*, 2444. [CrossRef]
59. Huang, Y.; Zhang, J.; Chen, D.; Qi, J. Model Reference Adaptive Control of Marine Permanent Magnet Propulsion Motor Based on Parameter Identification. *Electronics* **2022**, *11*, 1012. [CrossRef]
60. Karboua, D.; Mebkhouta, T.; Benkaihoul, S.; Chouiha, Y.; Toual, B.; Alqarni, Z.A.; Tazay, A.F.; Mosaad, M.I. Model reference adaptive system and Pseudo-Sliding Mode Control with Exponential Reaching Law for Sensorless-Speed control of PMSM. *PLoS ONE* **2025**, *20*, e0321985. [CrossRef]